Thin–Walled Structures 205 (2024) 112381

Contents lists available at ScienceDirect

Thin-Walled Structures

journal homepage: www.elsevier.com/locate/tws

# Clockwise vs anti-clockwise chiral metamaterials: Influence of base tessellation symmetry and rotational direction of chiralisation on mechanical properties

Luke Mizzi *, Luigi Grasselli, Andrea Spaggiari

*Department of Sciences and Methods for Engineering, University of Modena and Reggio Emilia, Reggio Emilia, Italy*

ARTICLE INFO

*Keywords:*
Chiral honeycombs
Auxetic metamaterials
Poisson's ratio
Euclidean polygonal tessellations
Hexagonal tilings
Pentagonal tilings

ABSTRACT

Chiral honeycombs are a class of auxetic metamaterials which are characterised by a lack of plane symmetry. Besides the traditional chiral honeycombs based on regular monohedral tessellations such as the hexachiral and tetrachiral honeycombs, a vast range of auxetic chiral metamaterials may be produced through the 'chiralisation' of Euclidean tessellations made from polyhedral tilings and/or irregular monohedral polygons. In this work, we show for the first time, how the direction of the geometric chiral transformation, i.e. clockwise vs anti-clockwise chiralisation, has an influence on the mechanical properties and deformation modes of the resultant chiral metamaterial systems. This influence, which is a result of the intrinsic absence of axial symmetry in the original base tessellation, can lead to the production of two unique and distinct chiral metamaterial configurations with completely different mechanical properties originating from a single base tessellation. In this work we demonstrate and quantify, through a wide range of numerical simulations and experimental tests on additively-manufactured prototypes, the effect of the direction of chiralisation on two tessellations: a Florent pentagonal system with hexagonal rotational symmetry and a hexagonal monohedral tessellation with trigonal rotational symmetry. The results obtained show that the clockwise and anti-clockwise chiral structures exhibit significantly different mechanical properties and deformation modes, highlighting the increased versatility of this relatively novel class of chiral metamaterials.

## 1. Introduction

Chiral honeycombs are one of the main classes of mechanical metamaterials with the capability of exhibiting a negative Poisson's ratio. This anomalous property, also known as auxeticity [1], imparts a number of useful accompanying characteristics to these metamaterials including a high indentation [2] and shear resistance [3] as well as the ability to adopt synclastic curvature [4]. These advanced functionalities make auxetic metamaterials ideal candidates for implementation in specialised applications such as biomedical implants, including stents [5], prosthesis [6] and skin grafts [7], as well as flexible electronics [8] and mechatronic components [9]. Chiral honeycombs, as their name implies, are systems which are characterised by an axi-asymmetric geometry which cannot be superimposed to its mirror image by rotations and translations alone. These systems deform primarily *via* rotation of nodes and flexure of ligaments and the first designed and most well-known example of such structures is the hexachiral honeycomb [10–17]. This system, first proposed by Wojciechowski [10] and later implemented in physical form by Prall and Lakes [11], possesses a Poisson's ratio of –1, has hexagonal rotational symmetry and exhibits transverse-isotropy. Since then, other chiral metamaterials have been realised including the tetrachiral [18–23] and trichiral [22,24,25] systems which are characterised by quadratic and trigonal rotational symmetry as well as variants with similar deformation modes but possessing one or multiple axes of symmetry, commonly known as anti-chiral [26–33] and meta-chiral [34] honeycombs. Additional chiral honeycombs based on polyhedral tessellations [35–40], hierarchical geometries [27] and 3D lattices [41–46] have also been designed and studied. Besides investigating the influence of the various geometric parameters such as chiral node size, ligament thicknesses and lengths on the Poisson's ratio of these systems, a number of studies have also analysed the effect of these dimensions on the stiffness and shear moduli as well as the out-of-plane curvature capabilities of these systems.

Despite this considerable number of works, there is one aspect of

* Corresponding author.
*E-mail address:* luke.mizzi@unimore.it (L. Mizzi).

https://doi.org/10.1016/j.tws.2024.112381
Received 22 May 2024; Received in revised form 23 August 2024; Accepted 23 August 2024
Available online 25 August 2024

these system which is commonly overlooked and, to the authors' knowledge, never examined deeply with respect to auxetic chiral metamaterials – the influence of the rotational direction of chirality on mechanical properties. As stated previously, chiral honeycombs are characterised by the absence of axial symmetry and, hence, as shown in Fig. 1, may be denoted either as clockwise or anti-clockwise chirals. Typically, the direction of chirality is not considered important and this is due to the fact that the current state-of-the-art on chiral honeycombs is primarily focused on systems based on regular hexagonal, quadrilateral and triangular monohedral tessellations, namely the aforementioned trichiral, tetrachiral and hexachiral honeycombs and their variants. The base tessellations of these systems all possess at least one axis of symmetry and, as a result of this, the chiralised counterparts of these tessellations are identical mirror-images of each other and exhibit the exact mechanical properties and deformation modes irrespective of whether clockwise or anti-clockwise chiralisation is applied. An example of this is shown in Fig. 1, where a clockwise and anti-clockwise trichiral system are illustrated. Both these systems are based on the same hexagonal tiling pattern, with the only difference being the direction of chiralisation.

However, this consideration only holds true if the original tessellation upon which the chiral honeycomb is based is axisymmetric. In the absence of axial symmetry, clockwise and anti-clockwise chiralisation of a completely asymmetric tessellation or a geometry which possesses only rotational symmetry results in two non-congruent chiral systems. Two examples of such tessellations are shown in Fig. 2. The first is a monohedral pentagonal tessellation [47,48] with rotational symmetry of order 6 (commonly known as a Florent pentagonal system) [49], while the second system is a monohedral hexagonal tessellation with trigonal rotational symmetry [47,48]. Both of these systems exhibit transverse isotropy (with or without chiralisation) due to their rotational symmetry characteristics [50,51]. It is evident from Fig. 2 that the corresponding clockwise and anti-clockwise chiralised structures derived from these tilings are unique and cannot be superimposed on each other. As a result of this, one would expect these systems to also deform in a different manner as well as exhibit diverse mechanical properties.

In this work, we aim to characterise and quantify the influence of the direction of chiralisation on the mechanical properties of chiral metamaterials based on axi-asymmetric tessellations. Through Finite Element simulations on a range of hexagonal and pentagonal tessellation-based chiral systems such as the ones shown in Fig. 2, as well as experimental loading tests on additively-manufactured prototypes, we show how the Poisson's ratio and Young's modulus of these metamaterials are affected by the relative directions of chiralisation and original rotational symmetry of the base tessellation.

## 2. Design of clockwise and anti-clockwise chiral honeycombs

In this section, we quantitatively define what constitutes clockwise and anti-clockwise chiralisation as well as geometric characteristics of the two base tessellations chosen for analysis.

### 2.1. Clockwise and anti-clockwise chiralisation

The chiralisation of a basic tessellation involves the formation of chiral nodes at the vertices of tessellation which are connected together through ligaments in an axi-asymmetric manner. Typically, circular chiral nodes are used and they are connected to each other through tangentially-attached ligaments as shown in Fig. 3a. If we consider two adjacent vertices of a hypothetical tessellation, A and B, which are distant from each other by a length $R$ (defined by the original base tessellation geometry), then the chiralisation of these two points may be defined in terms of two additional independent geometric variables. These two variables are the node radius, $r$, and the ligament thickness, $t$. The resultant ligament length, $l$, is a dependent variable, which may be

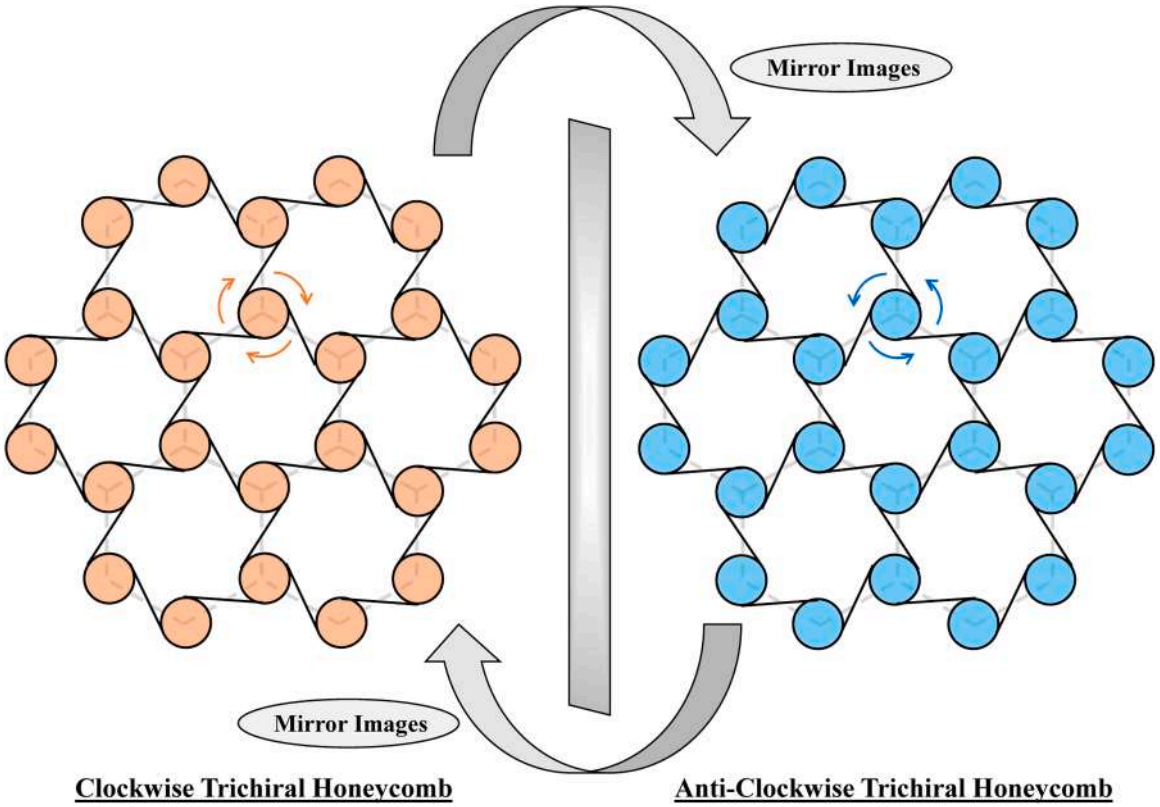


**Fig. 1.** A regular trichiral honeycomb with the chiral nodes connected in a clockwise and anti-clockwise manner. The two systems are identical mirror-images of each other.

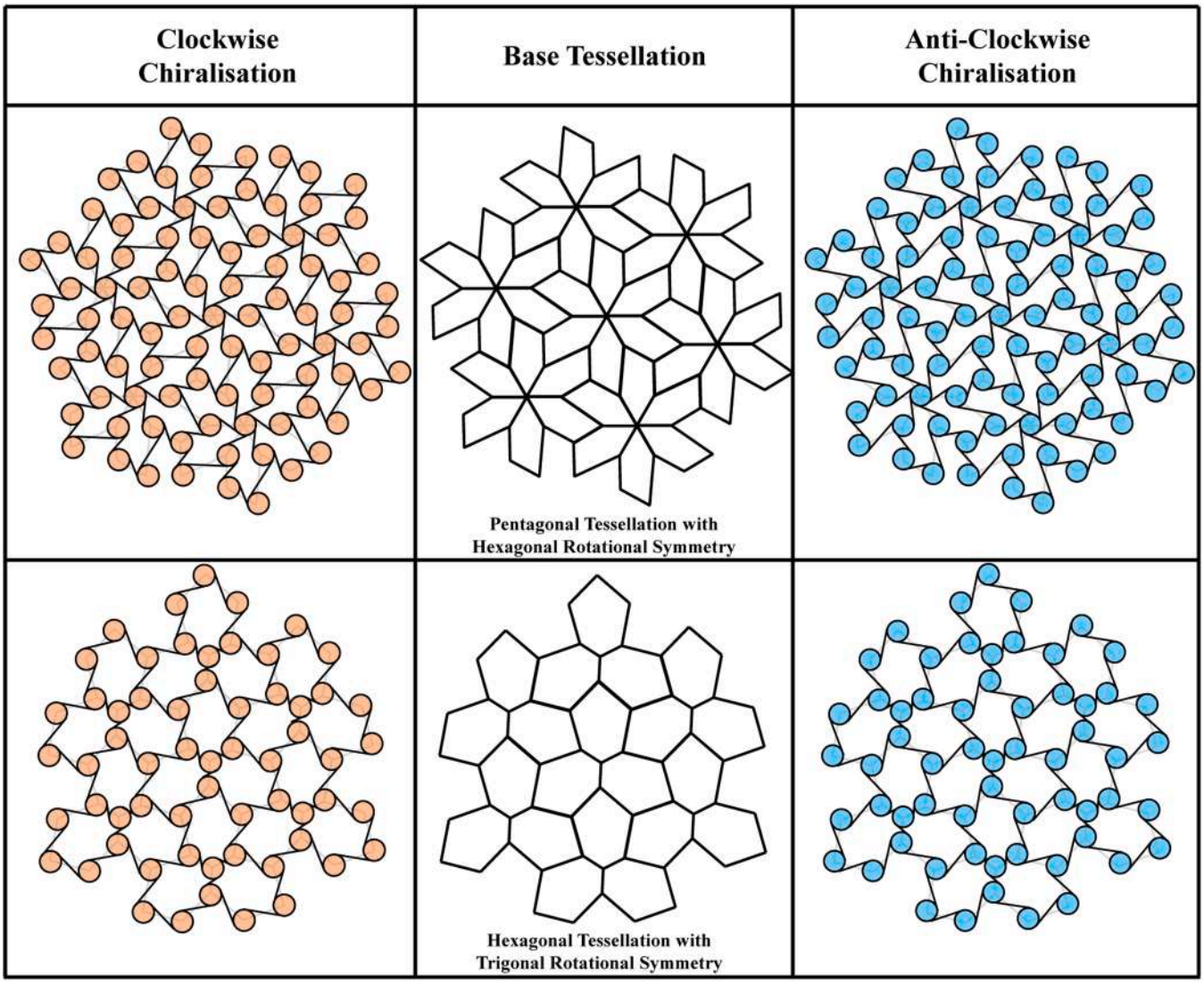


**Fig. 2.** Clockwise and anti-clockwise chiralisation of a pentagonal tessellation with hexagonal rotational symmetry (Florent pentagonal tessellation) and a hexagonal tessellation with trigonal rotational symmetry. It is evident that the resultant chiral honeycombs in each case are unique and cannot be super-imposed upon each other.

determined as a function of $R$, $r$ and $t$ as follows:

$$l = 2\sqrt{\left(\frac{R}{2}\right)^2 - \left(r - \frac{t}{2}\right)^2} \tag{1}$$

Besides these variables, there is also another geometric factor which must be considered; the direction of chiralisation. As shown i ligament with length $l$ may be tangentially connected to the chiral nodes in two ways; through a clockwise or anti-clockwise rotational direction. These two forms of chiralisation may be geometrically defined as follows:

- *Clockwise Chiralisation* – Taking into account the tangent point (T) of the ligament with the chiral node, the radius AT is superimposed on the $x$-axis through an in-plane rotation of an angle less than 90° in the *clockwise* direction.
- *Anti-Clockwise Chiralisation* – Taking into account the tangent point (T) of the ligament with the chiral node, the radius AT is superimposed on the $x$-axis through an in-plane rotation of an angle less than 90° in the *anti-clockwise* direction.

### 2.2. Pentagonal and hexagonal tessellations

As shown in Fig. 2, two tessellations which are characterised solely by a planar rotational symmetry of order $n$ were investigated; namely the Florent pentagonal tiling (with rotational symmetry of order 6) and the chosen hexagonal tiling (with a rotational symmetry of order 3). The main reason why these two geometries were chosen is that they both allow for considerable geometric variation whilst retaining their underlying rotational symmetry characteristics which includes both convex and concave configurations. This geometric versatility therefore allows one to examine the influence of base tessellation parameters and direction of chiralisation on mechanical properties while keeping the rotational symmetry of the overall system unchanged. In this section, a brief overview on the design of the base tessellations is provided.

#### 2.2.1. Pentagonal tessellation with hexagonal symmetry

This particular pentagonal tessellation (also known as a Florent pentagonal tiling) is characterised by a rotational symmetry of order 6 and can be defined by three independent geometric variables: $i$, $j$ and $k$, shown in Fig. 4. The tessellation considered in this work may be designed by constructing two external triangles adjacent to a generic

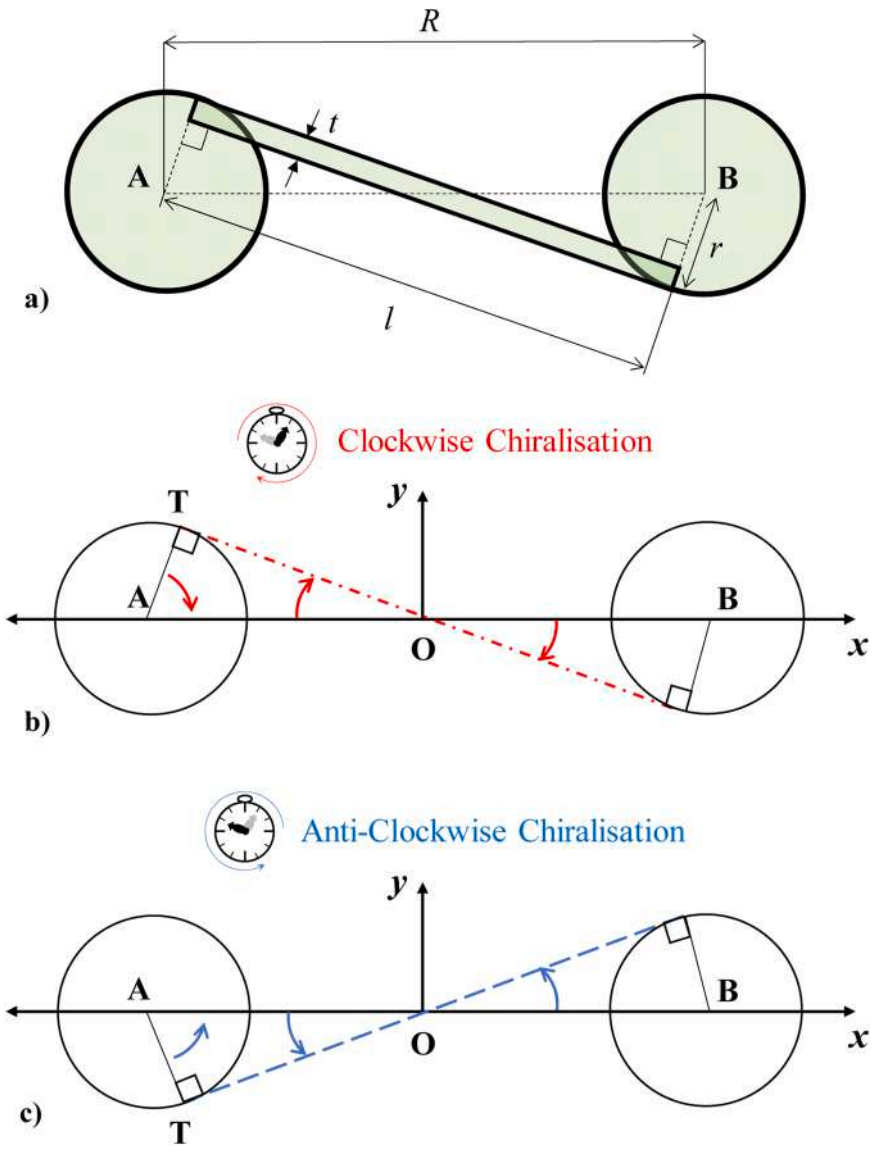


**Fig. 3. a).** Formation of chiral nodes and connecting ligament between two points, A and B along with resultant geometric parameters. Schematics showing how the ligament can be formed in a b) clockwise and c) anti-clockwise rotational direction.

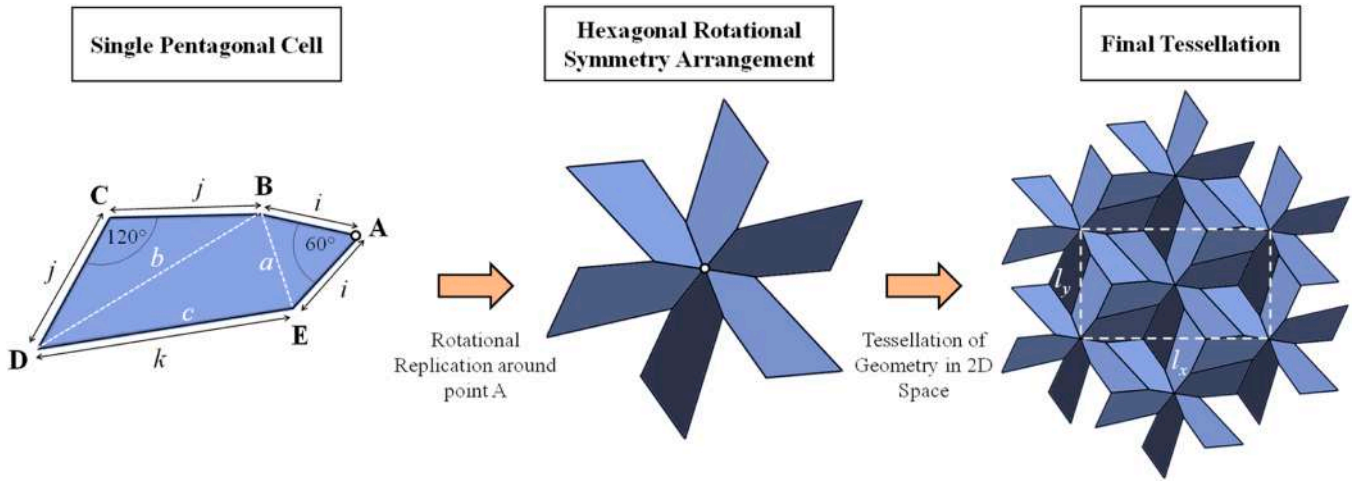


**Fig. 4.** Design of the Florent pentagonal tessellation. The dashed white lines show the rectangular representative unit cell of the system.

triangle with sides of lengths *a, b* and *c* (see Fig. 4) on sides *a* and *b*. The triangle constructed from the side of length *a* is an equilateral triangle, while the one constructed from side *b* is an isosceles triangle with an internal angle of 120°. The lengths *a, b* and *c* are related to the external side lengths of the pentagon as follows: $a = i$, $b = j\sqrt{3}$ and $c = k$ and therefore, for any chosen set of *i, j* and *k* to result in a realisable tessellation, the following conditions must be met:

a. The angle between the two sides with length *i* must be equal to 60°
b. The angle between the two sides with length *j* must be equal to 120°
c. The chosen combination of side lengths *i, j* and *k* must respect the following triangle realisability condition:

$$\left|\frac{i^2 + 3j^2 - k^2}{2ij\sqrt{3}}\right| < 1 \tag{2}$$

As stated previously, these existence limits permit the design of various configurations including both convex and concave ones. For the sake of brevity, we have omitted to include a detailed explanation on the design of these tilings and refer the reader to [40] for a more in-depth analysis on the mathematical conditions necessary for all the permissible forms of convex and concave systems. Given that the tessellation is known to be transversely isotropic, due its inherent hexagonal rotational symmetry [51], the choice of orientation for the representative unit cell (RUC) with respect to the global cartesian coordinate system is of no consequence with regards to the mechanical properties obtained for the system and, therefore, the rectangular cell based on the 6-fold rotational symmetry points of the tessellated structure was chosen for convenience. This unit cell has the following dimensions, $l_x$ and $l_y$, which are defined as follows:

$$l_x = \sqrt{3} l_y \tag{3}$$

$$l_y = 2\sqrt{i^2 + \frac{k^2}{4} - ik\cos\left[\arccos\left(\frac{i^2 + k^2 - 3j^2}{2ik}\right) + \frac{\pi}{3}\right]} \tag{4}$$

### 2.2.2. Hexagonal honeycomb with trigonal symmetry

The hexagonal honeycomb with trigonal symmetry, shown in Fig. 5, may also be defined by three independent length variables: the three side length parameters: *i, j* and *k*. In analogy with the pentagonal tessellation, this Euclidean tiling can also be designed from an internal triangle with side lengths *a, b* and *c*. In this case, isosceles triangles with an angle of 120° are constructed externally on all three sides. The lengths of the internal triangle are related to the hexagon parameters as follows: $a = i\sqrt{3}$, $b = j\sqrt{3}$ and $c = k\sqrt{3}$ and the conditions to design these tessellations are:

a. The angles between the three pairs of sides with equal lengths must be equal to 120°
b. The chosen combination of side lengths *i, j* and *k* must respect the triangle realisability condition:

$$\left|\frac{i^2 + j^2 - k^2}{2ij}\right| < 1 \tag{5}$$

These conditions permit the design of both concave and convex tessellation, with a concave tessellation being formed if one of the angles of the triangle with sides *a, b* and *c* exceeds 120°. As shown in Fig. 5, a rectangular unit cell was chosen for these systems with dimensions $l_x$ and $l_y$, which are defined as follows:

$$l_x = \sqrt{i^2 + k^2 - 2ik\cos\left(\arccos\left(\frac{i^2 + k^2 - j^2}{2ik}\right) + \frac{\pi}{3}\right)} + \sqrt{i^2 + j^2 - 2ij\cos\left(\arccos\left(\frac{i^2 + j^2 - k^2}{2ij}\right) + \frac{\pi}{3}\right)} + \sqrt{j^2 + k^2 - 2jk\cos\left(\arccos\left(\frac{j^2 + k^2 - i^2}{2jk}\right) + \frac{\pi}{3}\right)} \tag{6}$$

$$l_y = \frac{l_x}{\sqrt{3}} \tag{7}$$

Since this tessellation exhibits trigonal rotational symmetry, it is also analytically predicted to exhibit transverse isotropy [51] and thus the chosen orientation of the representative unit cell has no bearing on the resultant mechanical properties (neither before nor after chiralisation).

## 2.3. Chiralisation of tessellations

As shown in Fig. 2, the chiralisation of these tessellations is essentially performed by forming chiral nodes at the vertices of the polygons and connecting them through clockwise or anti-clockwise oriented tangentially-attached ligaments. Naturally, this transformation entails

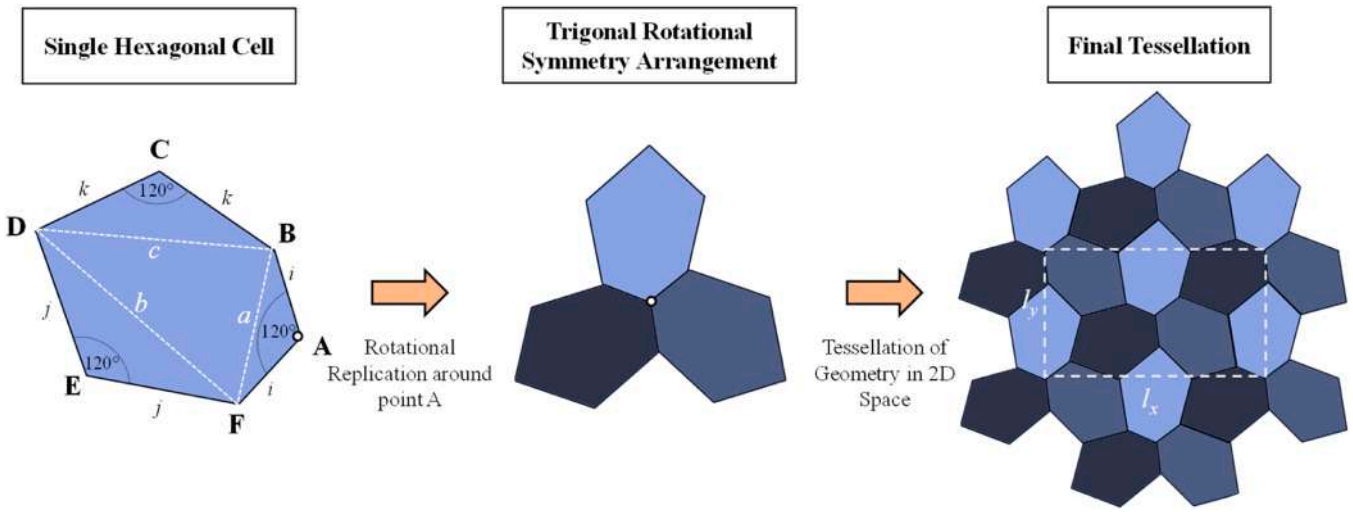


**Fig. 5.** Design of the hexagonal tessellation with trigonal rotational symmetry. The dashed white lines show the rectangular representative unit cell of the system.

additional geometric restrictions on the realisability of these chiral honeycombs further to the original tessellation constraints indicated in Eqs. 2 and 5. The most obvious restriction is that the chiral node radii must be small enough with respect to the original tessellation side length so as to ensure that a ligament may be formed between two adjacent connected nodes. In this case, a uniform node radius dimension, $r$, was used and thus this geometric condition, which is valid for both tessellations, can be expressed as follows:

$$\frac{r}{2} < i, j, k \tag{8}$$

This condition is sufficient for all configurations of the hexagonal tessellations with trigonal rotational symmetry described in Section 2.2.2, however, in the case of the pentagonal tessellations with hexagonal rotational symmetry, there is an additional geometric constraint which must be met in the case of concave systems. This condition, which ensures that the ligaments of the chiral honeycomb do not intersect with nodes to which they are not supposed to be connected, depends highly on direction of chiralisation. For clockwise chiralisation, the condition is as follows:

$$i\cos(\theta+\beta) < -t \tag{9}$$

while for anti-clockwise:

$$i\cos(\theta-\beta) > 2r \tag{10}$$

The full explanation and derivation of these conditions, along with the definition of the variables $\theta$ and $\beta$, is presented in Appendix 1.

## 3. Methodology

In order to study the influence of direction of chiralisation on the mechanical properties of these metamaterials, two approaches were used. First, a parametric analysis was conducted using Finite Element (FE) simulations under linear loading and periodic boundary conditions on five configurations representative of typical convex and concave systems of each tessellation type. This was then followed by experimental tests on a number of 3D-printed prototypes in order to analyse the behaviour of these systems at small strain loading and validate the results obtained from the initial parametric run.

### 3.1. Parametric analysis using linear FE simulations

The ten tessellations investigated in this work are illustrated in Fig. 6 and listed in Table 1. These tessellations encompass representative configurations of both convex and concave pentagons and hexagons and were chiralised by forming circular nodes at the vertices of the polygons and tangentially-connected ligaments. The geometric chiralisation variables, the node radius, $r$, and the ligament thickness, $t$ (see Fig. 3a), were varied as follows: $r$ was set at a range between 0.5 mm and 5 mm with steps of 0.5 mm, while $t$ was varied from 0.1 mm to 1.0 mm in steps of 0.1 mm. Since 10 systems were studied and each structure was constructed in the form of a clockwise chiralised and anti-clockwise chiralised variant, the resultant factorial space yields a total of 2000 chiral structures. In reality, the actual number of simulated systems was slightly lower than this value due to the geometric conditions indicated in Eqs. 8–10, rendering certain combination of variables inadmissible, since they result in unrealisable configurations.

In order to find the Poisson's ratio and Young's modulus of these chiral systems, FE simulations were conducted using the ANSYS16 software. The systems were constructed as planar, single representative unit cells and simulated under periodic boundary conditions. PLANE183, a higher order 2-D, mixed 8-node or 6-node element with

**Table 1**
Dimensions of tessellations studied in this work and shown in Fig. 6.

| Pentagonal tessellations | | | | | |
|---|---|---|---|---|---|
| Tessellation | $i$ (mm) | $j$ (mm) | $k$ (mm) | $j/i$ | $k/i$ |
| P1 | 24.0 | 7.2 | 28.8 | 0.3 | 1.2 |
| P2 | 24.0 | 12.0 | 7.2 | 0.5 | 0.3 |
| P3 | 24.0 | 24.0 | 24.0 | 1.0 | 1.0 |
| P4 | 24.0 | 19.2 | 19.2 | 0.8 | 0.8 |
| P5 | 24.0 | 28.8 | 33.6 | 1.2 | 1.4 |
| Hexagonal tessellations | | | | | |
| Tessellation | $i$ (mm) | $j$ (mm) | $k$ (mm) | $j/i$ | $k/i$ |
| H1 | 24.0 | 19.2 | 14.4 | 0.8 | 0.6 |
| H2 | 24.0 | 36.0 | 12.0 | 1.5 | 0.5 |
| H3 | 24.0 | 14.4 | 9.6 | 0.6 | 0.4 |
| H4 | 24.0 | 38.4 | 16.8 | 1.6 | 0.7 |
| H5 | 24.0 | 43.2 | 19.2 | 1.8 | 0.8 |

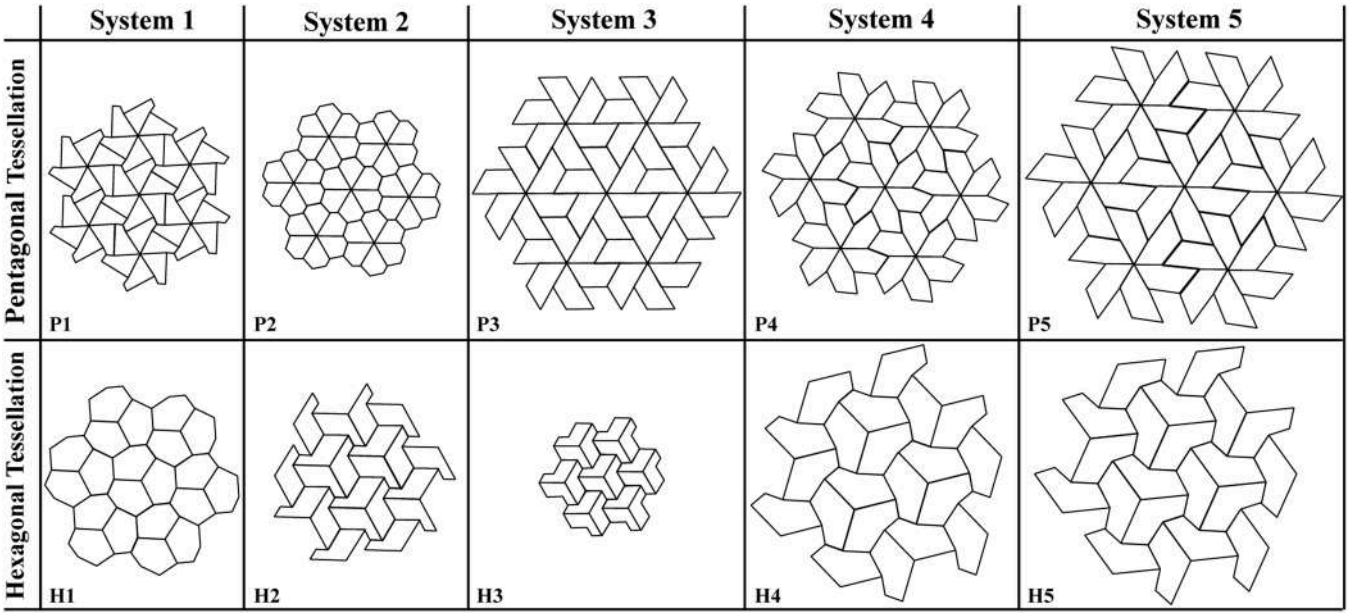


**Fig. 6.** Schematic showing the five pentagonal and five hexagonal tessellations which were chiralised and investigated in this study. The systems are presented to scale relative to one another in order to allow for a visual comparative analysis. The dimensions of these tessellations are listed in Table 1.

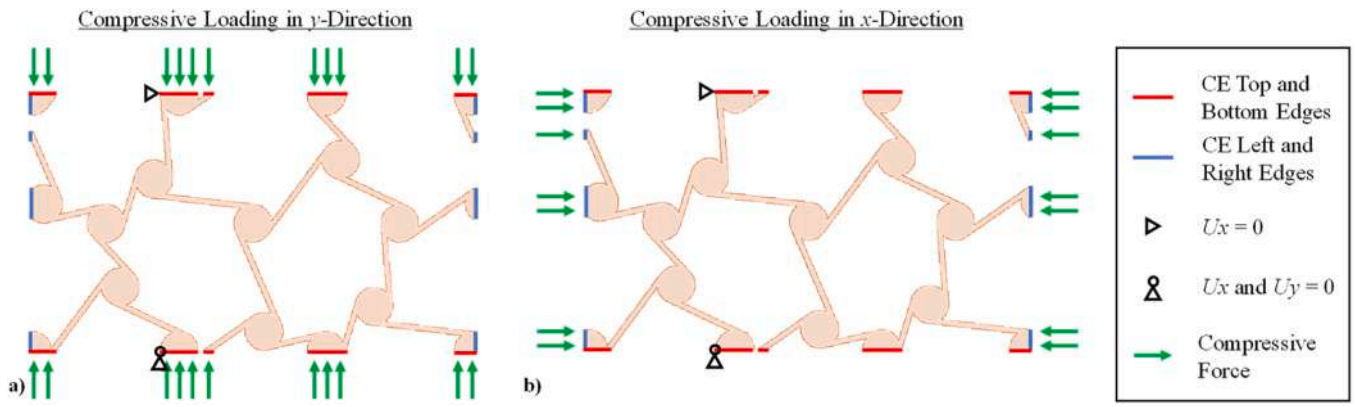


**Fig. 7.** Illustration indicating the loading modes employed to simulate uniaxial compression of a representative unit cell of the H1 tessellation in the a) *y*- and b) *x*-directions. The red and blue lines indicated nodes paired by constraint equations. The system was fixed from only two corresponding nodes on the horizontal boundaries and uniaxial compressive force loading was employed. This generic implementation of periodicity ensures that the axially asymmetric unit cell can deform freely.

quadratic displacement behaviour and two degrees of freedom, was used under plane-stress conditions. Following convergence tests, the minimum mesh size was set to $t_{min}/4$, where $t_{min}$ is the minimum ligament thickness, i.e. 0.1 mm. Naturally, for systems with thicker ligaments, larger elements were used in order to minimise the computational time (following additional mesh size convergence testing). The material properties of isotropic ABS plastic were used: Poisson's ratio of 0.3 and Young's modulus of 2 GPa. In order to specify the periodic boundary conditions, constraint equations were applied on the nodes on the edges of the unit cells. These constraint equations pair nodes on opposing edges and ensure that the displacements in the *x*- and *y*-directions of edge nodes are mirrored by the nodes on the opposing edge. The system is fixed from a single point in the *x*- and *y*-direction at the bottom edge and fixed in the *x*-direction only from the corresponding point on the top edge as shown in Fig. 7. This ensures that the system remains aligned with the *y*-axis throughout deformation. Uniaxial loading is applied through the application of a compressive force on opposing edges of the representative unit cell. The systems were loaded separately in both the *x*- and *y*-directions under linear elastic loading conditions and the Poisson's ratios and effective Young's moduli were extracted. Further information on the simulation methodology used may be found in [52].

### 3.2. Experimental tests

In order to experimentally validate the numerical simulation results, two pairs of chiral pentagonal and hexagonal tessellations were fabricated using a Fused-Deposition Method (FDM) 3D-Printer in ABS plastic. The dimensions and relative parameters of these systems, which correspond to the P2 and H2 configurations respectively, were chosen on the basis of the results obtained from the parametric study described in the previous section and the design constraints imposed by the 3D-printer resolution and platform space. Both pentagonal and hexagonal chiral systems were designed as 3×5 representative unit cells with an out-of-plane thickness of 20 mm. The systems are shown in Fig. 8, while the parameters are listed in Table 2.

These structures were each subjected to uniaxial *quasi*-static compressive loading tests using a Galdabini® Sun 500 tensile loading machine with a 5kN Loadcell. A global compressive displacement of 8 mm, equivalent to *ca.* 4 % strain in the *y*-direction was applied at a rate of 2 mm/min. In order to measure the Poisson's ratio of these systems, a Digital Imaging Correlation system was used to track the deformation of the central RUC of each structure (see Fig. 8). A camera was focused on the central RUC and the four corners of the unit cell were tracked in order to measure the displacements at each frame. Naturally, being a finite system influenced by edge effects, the deformation of the central unit cell is not equivalent to the deformation of the overall global system and, therefore, the central unit cell deforms significantly less than the 4 % globally imposed strain.

## 4. Results and discussion

The results showing the Poisson's ratios, $\nu$, obtained from the parametric study using linear FE simulations for the pentagonal and hexagonal tessellation-based chiral systems are presented in Figs. 9 and 10 respectively. The values obtained for loading in the *x*- and *y*-directions were identical, as expected since the symmetry characteristics of these metamaterials impart in-plane isotropic behaviour, and thus the results shown in the plots represent the isotropic Poisson's ratio of these systems.

It is clearly evident from the plots that chiralisation has a distinct influence on the mechanical properties of these tessellation geometries. The general trend in nearly all systems is that the Poisson's ratio decreases as the degree of chiralisation increases, i.e. as $r$ increases and $t$ decreases, with the lowest Poisson's ratios being generally observed for systems with $r = 5$ mm and $t = 0.1$ mm. This effect is particularly pronounced in the case of pentagonal tessellations, with the clockwise P2 tessellation exhibiting almost the entire spectrum of permissible transverse isotropic Poisson's ratio with values ranging from +0.95 to –0.96. On the other hand, the influence of chiralisation on the Poisson's ratio of the hexagonal tessellations is less drastic and, although it decreases appreciably, the reduction is less noticeable. Despite this reduced influence, chiral systems based on hexagonal tessellations still possess the capability of exhibiting auxetic behaviour as evidenced by the plots for systems H3 and H5.

It is also manifestly clear that the rotational direction of chiralisation is an extremely influential and important factor in determining the mechanical properties of these systems. In all systems, with the exception of H1 and H4 tessellations, the Poisson's ratios of the clockwise and anti-clockwise chiralised systems are different. In some cases, this difference is exceedingly prominent. Tessellation P2 is a case in point, where the highly chiralised clockwise tessellations exhibit decidedly negative Poisson's ratios, while the corresponding anti-clockwise chiral systems show Poisson's ratio close to zero. An example is shown in Fig. 11, where the deformation of the clockwise and anti-clockwise chiralised P2 systems with the parameters $t = 0.2$ mm and $r = 3.5$ mm are demonstrated. These systems exhibited Poisson's ratios of –0.96 and –0.06 respectively and it is clearly evident that they exhibit different deformation modes. While in the clockwise chiralised system, the deformation is almost entirely absorbed by the six long ligaments connected to the central chiral node, causing it to rotate, in the anti-clockwise system, significant deformation can also be observed on the shorter ligaments, while the deformation of the six long ligaments is not

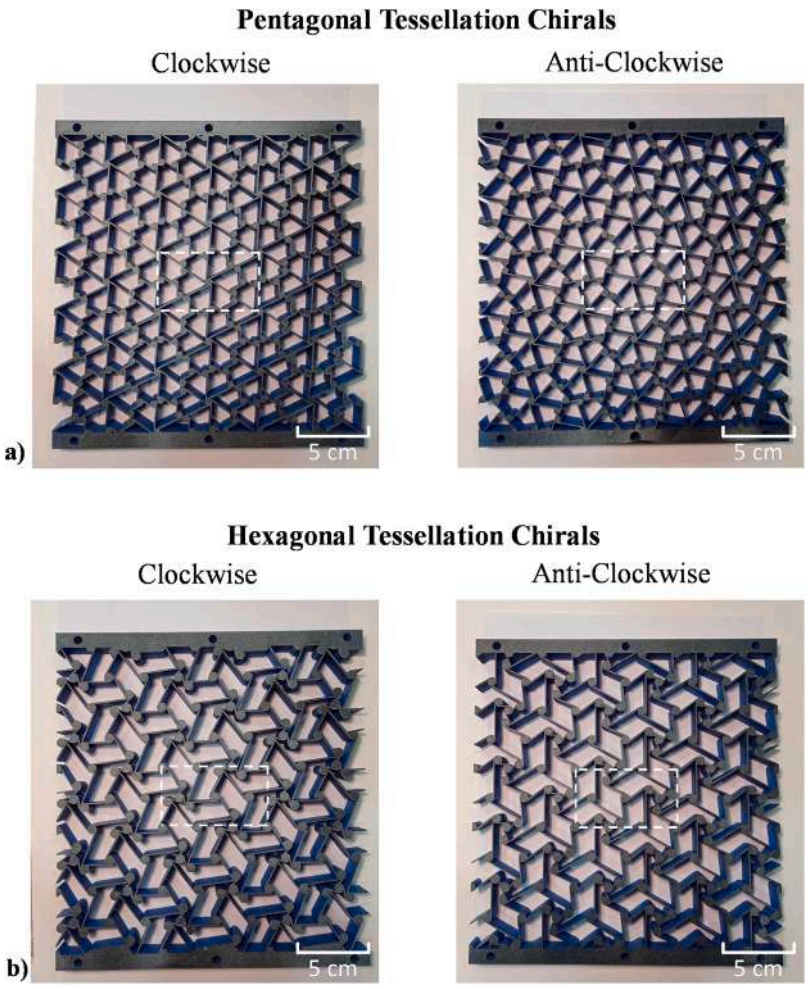


**Fig. 8.** Images showing the additively-manufactured a) Pentagonal Tessellation-based chirals (P2) and b) Hexagonal Tessellation-based chirals (H2) with the design parameters listed in Table 2. The white dashed lines indicate the central RUC tracked using the DIC method in order to measure the Poisson's ratio.

**Table 2**
Dimensions 3D printed prototypes shown in Fig. 8. RUC represents the number of representative unit cells in the $x$ and $y$-directions used for the finite system, while $L_x$ and $L_y$ indicate the total gauge length of the finite system in the $x$ and $y$-directions respectively.

| Pentagonal tessellation P2 (clockwise and anti-clockwise) | | | | | | | | |
|---|---|---|---|---|---|---|---|---|
| $i$ (mm) | $j$ (mm) | $k$ (mm) | $t$ (mm) | $r$ (mm) | $RUC_x$ | $RUC_y$ | $L_x$ (mm) | $L_y$ (mm) |
| 19.20 | 9.60 | 5.76 | 1.00 | 2.4 | 3 | 5 | 214.12 | 206.04 |
| Hexagonal Tessellation H2 (Clockwise and Anti-Clockwise) | | | | | | | | |
| $i$ (mm) | $j$ (mm) | $k$ (mm) | $t$ (mm) | $r$ (mm) | $RUC_x$ | $RUC_y$ | $L_x$ (mm) | $L_y$ (mm) |
| 18.00 | 27.00 | 9.00 | 1.00 | 3.2 | 3 | 5 | 214.31 | 206.22 |

identical for each one.

The example shown in Fig. 11 represents one of the most extreme cases with respect to the differences between clockwise and anti-clockwise chiralised systems. In the other systems, the differences are less acute, but still significant. For tessellation P1, highly chiralised systems in the clockwise direction exhibited Poisson's ratios with values as low as –0.82 while the corresponding anti-clockwise metamaterials systems showed Poisson's ratios of around –0.68. On the other hand for tessellation P3, the Poisson's ratio ranged from +0.31 to +0.22 for the clockwise chiralised systems and +0.28 to +0.03 for the anti-clockwise chiralised systems. It was also observed that there appears to be no trend with respect to whether clockwise or anti-clockwise chiralisation is most conducive to auxetic behaviour. In the case of pentagons, while clockwise chiralised P1 and P2 tessellations are observed to exhibit more auxetic behaviour with respect to their anti-clockwise counterparts (with this trend also being observed for the non-auxetic P4 systems), anti-clockwise P3 and P5 tessellations were generally found to possess lower Poisson's ratios than the corresponding clockwise chiral systems.

The same effect was observed for the hexagonal tessellations, albeit at a far less pronounced level. While the lowest Poisson's ratios for systems H2, H4 and H5 were found for the most highly chiralised anti-clockwise systems, for H3 the most auxetic values were obtained for the clockwise chiralised systems. In general, it appears as though the mechanical properties of the hexagonal tessellations are considerably less influenced by chiralisation in comparison to pentagonal tessellations, with the variations in magnitude of Poisson's ratio being relatively small. This factor is probably the reason why there is so little difference between clockwise and anti-clockwise chiralised systems; i.e. if chiralisation has very little influence on the deformation mechanism of these systems, then the direction of chiralisation is also expected to have a

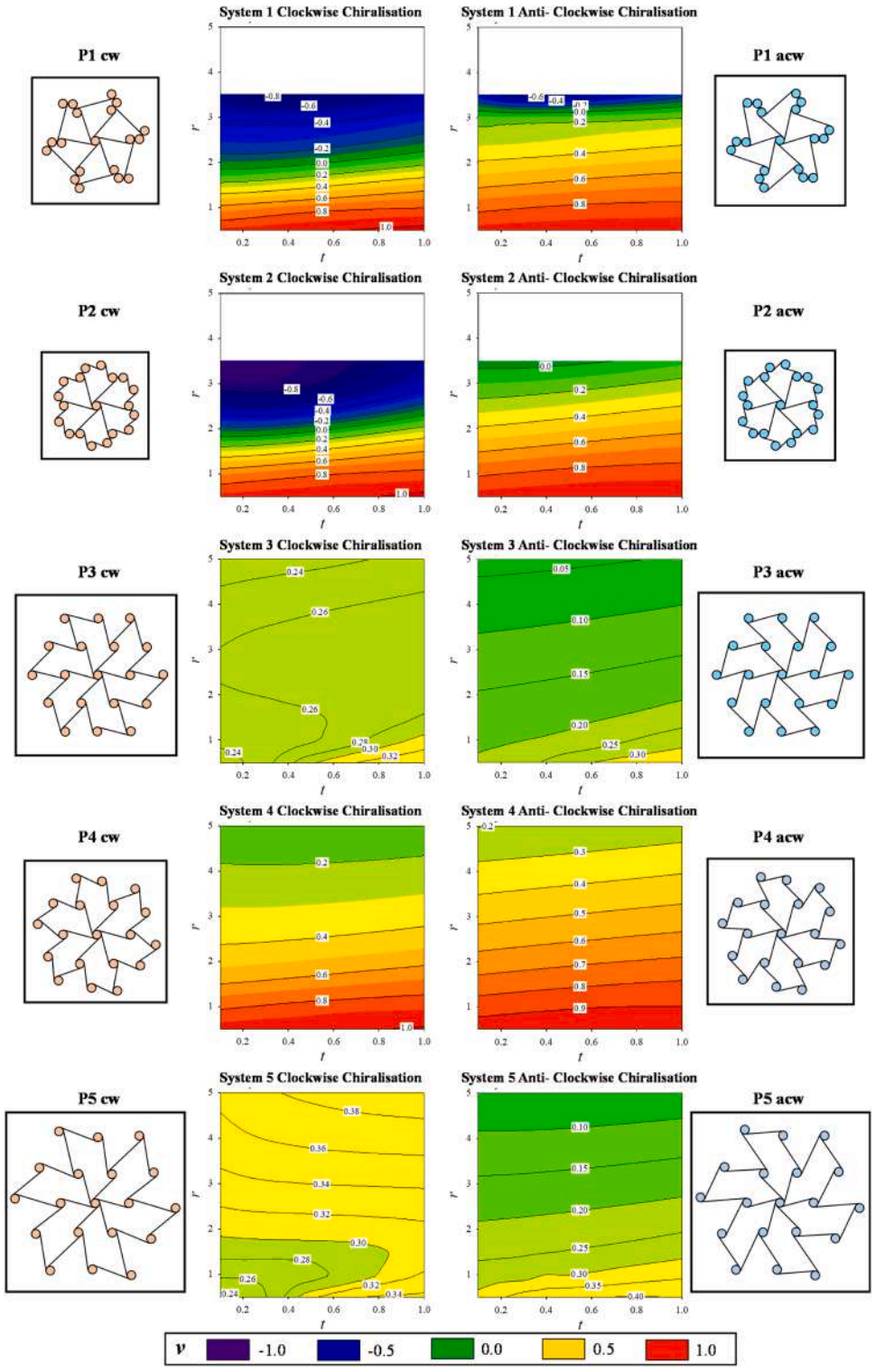


**Fig. 9.** Plots showing how the Poisson's ratio, $\nu$, varies with changing $t$ and $r$ for clockwise (cw) and anti-clockwise (acw) chiralised pentagonal tessellations. The white space in the first four plots represents unrealisable geometries.

slight effect. A case in point is system H1, where there is almost no difference in the mechanical properties of the clockwise and anti-clockwise systems. It is evident from Fig. 12 that these systems exhibit similar deformation modes and hence, very similar Poisson's ratios. There is also no visible rotation of chiral nodes as observed for the pentagonal tessellations. However, despite the reduced influence of chiralisation, hexagonal tessellations still possess the capability of exhibiting auxetic behaviour with configurations such as H2, H3 and H5 showing negative Poisson's ratios.

Similar observations were also evident from the results of the effective Young's modulus, $E^*$, of these systems. This property, which is a ratio defined as the metamaterial Young's modulus ($E_{meta}$, Young's modulus obtained from the FE simulation) divided by the constituent material Young's modulus ($E_{mat}$, material Young's modulus utilised to run the FE simulation) is a unitless parameter which is characteristic of the metamaterial geometry itself, independent of constituent material

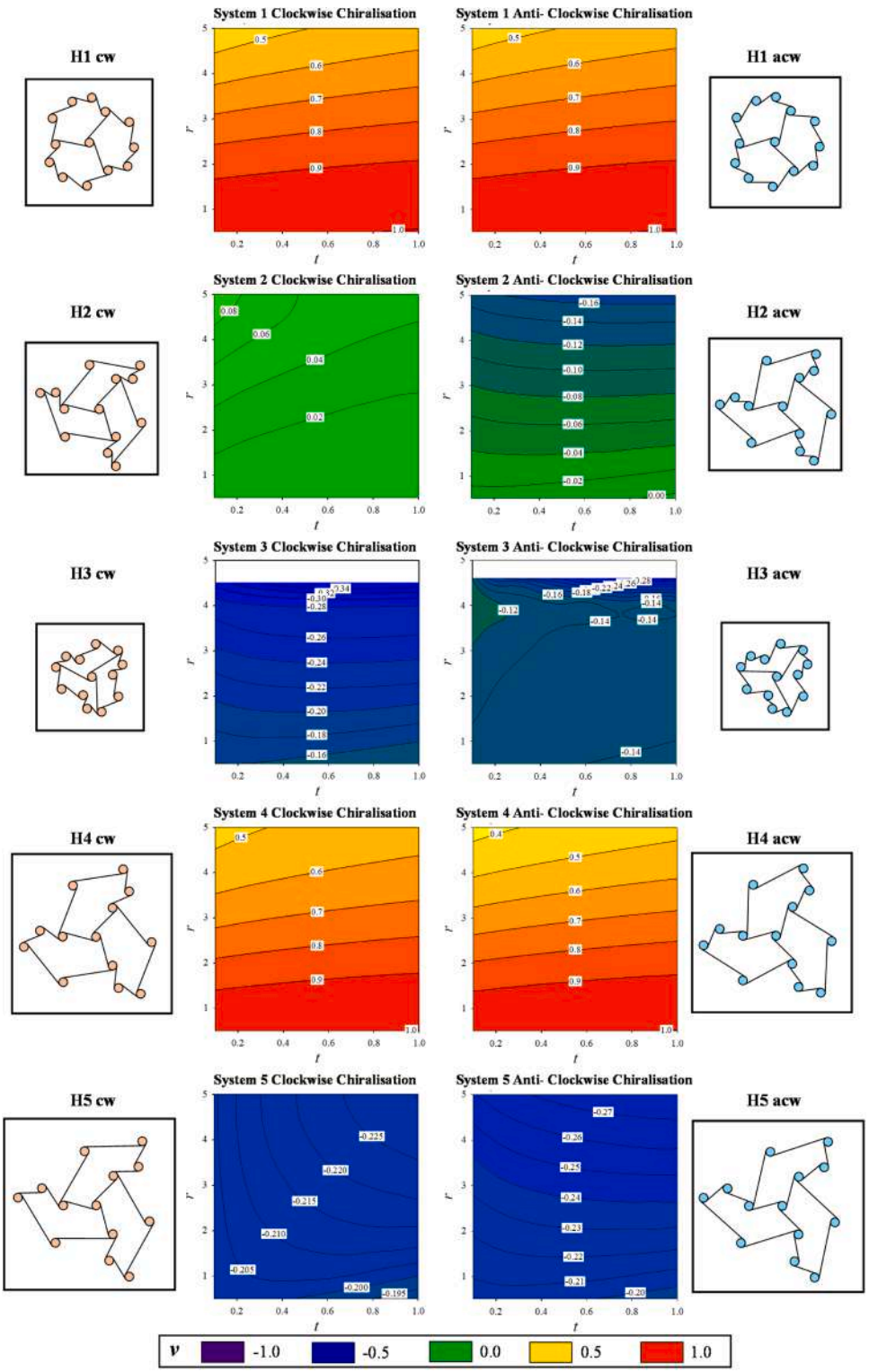


**Fig. 10.** Plots showing how the Poisson's ratio, $\nu$, varies with changing $t$ and $r$ for clockwise (cw) and anti-clockwise (acw) chiralised hexagonal tessellations. The white space in the fifth and sixth plot represents unrealisable geometries.

used. The values obtained for all systems investigated in this work are presented in Figs. 13 and 14. In this case, the differences are more difficult to observe due to the fact that the effective Young's modulus increases exponentially upon increasing ligament thickness. However, it is still clearly evident that there are differences between the clockwise and anti-clockwise chiralised systems, particularly in the case of the pentagonal tessellations. For the hexagonal systems, the differences are less visible except perhaps in the case of H3 where the anti-clockwise chiralised systems exhibit considerably higher effective Young's modulus in comparison to their clockwise counterparts. In the case of H1 and H2, the effective Young's moduli for both directions of chiralisation are identical, highlighting the fact that the deformation mechanism is extremely similar in both cases.

The trends observed from the parametric study between clockwise

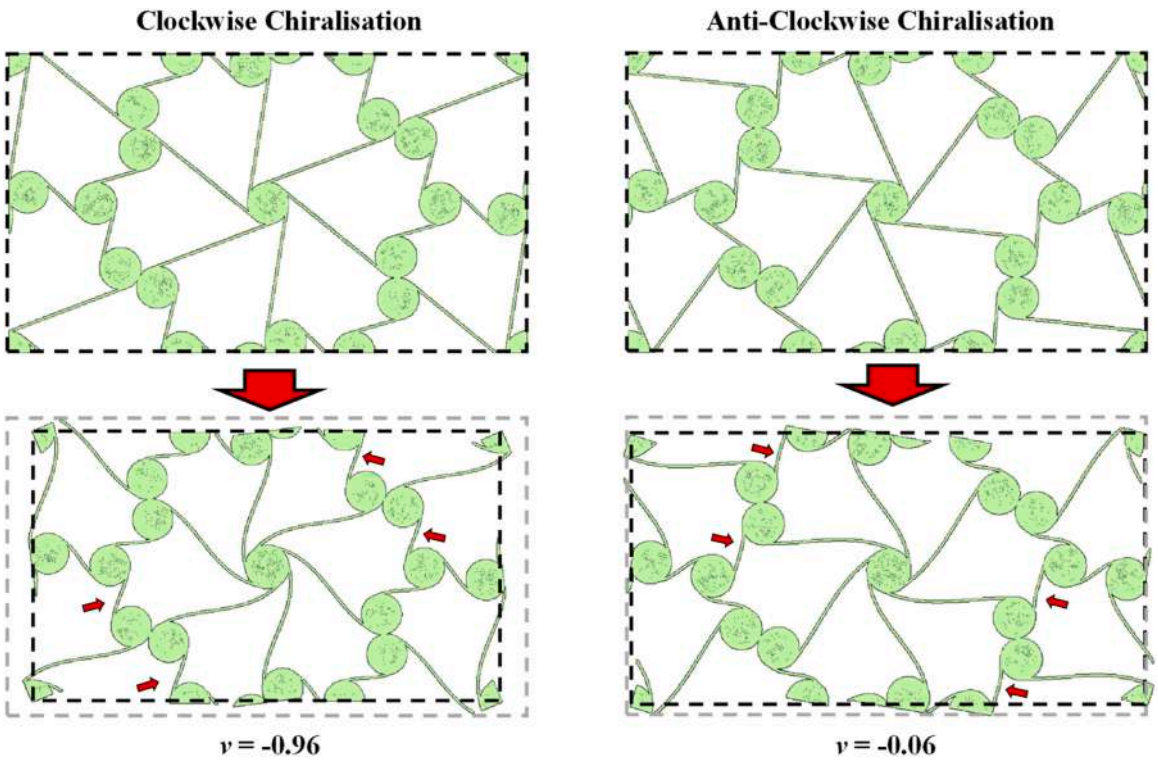


**Fig. 11.** Images showing the undeformed and deformed P2 systems with $r = 3.5$ mm and $t = 0.2$ mm and clockwise and anti-clockwise chiralisation subjected to compressive loading in the $y$-direction. The deformation is magnified through displacement scaling of the solution obtained from the linear simulations. The small red arrows indicate the small *quasi*-vertical ligaments in both systems; it is evident that in their deformation is greater in the anti-clockwise system in comparison to the corresponding clockwise system.

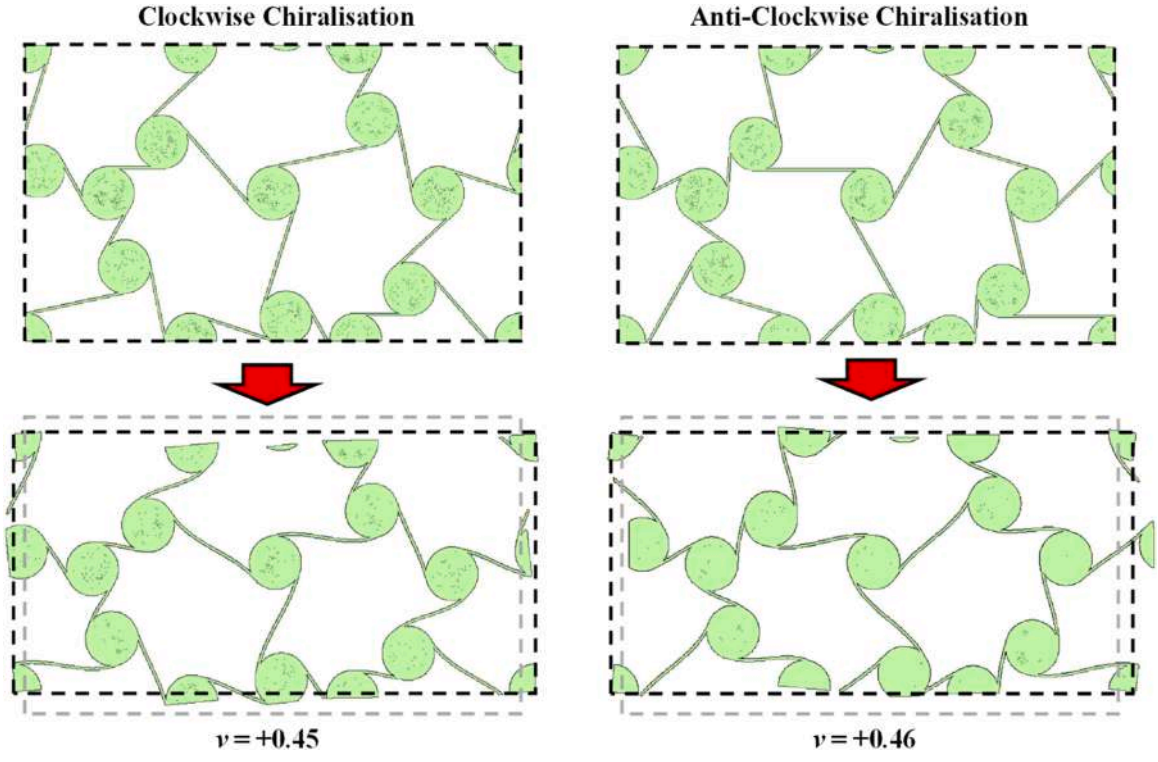


**Fig. 12.** Images showing the undeformed and deformed H1 systems with $r = 5.0$ mm and $t = 0.2$ mm and clockwise and anti-clockwise chiralisation subjected to compressive loading in the $y$-direction. The deformation is magnified through displacement scaling of the solution obtained from the linear simulations.

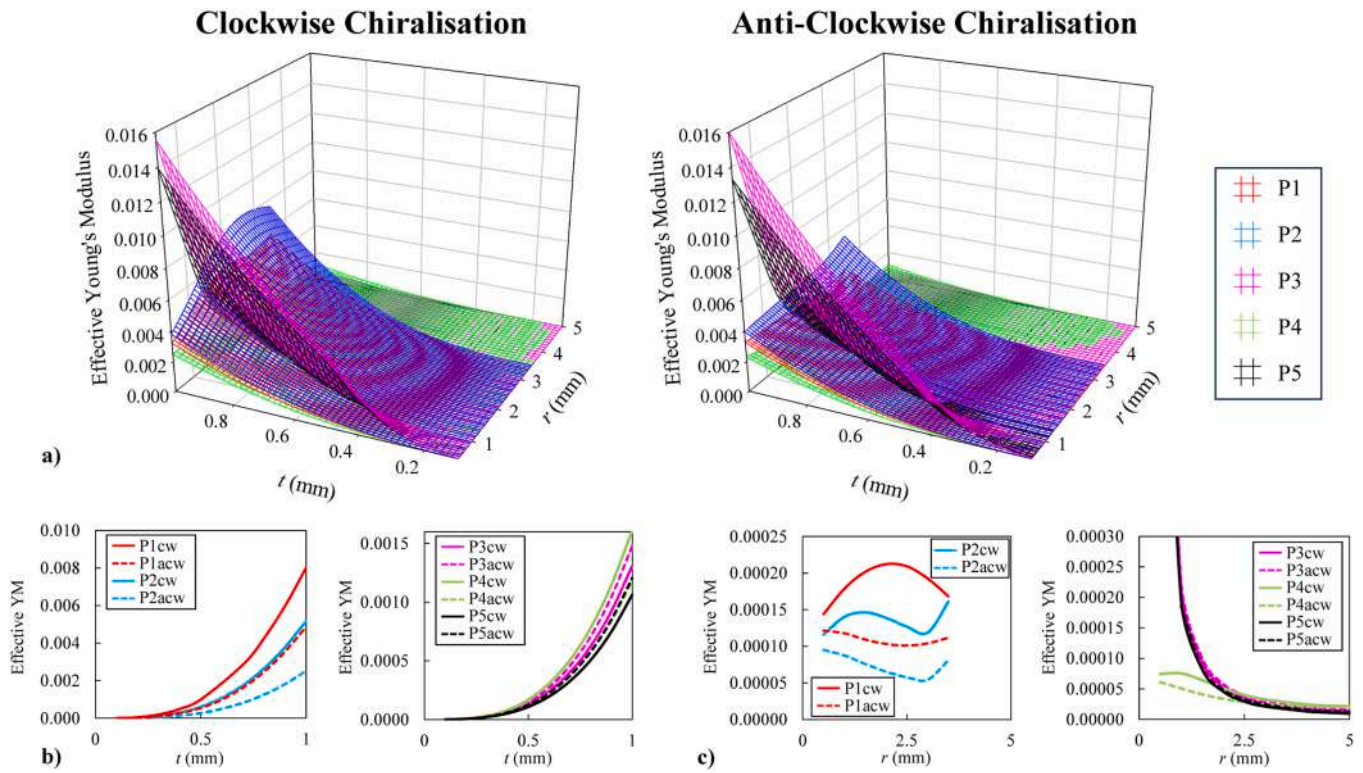


**Fig. 13. a).** Plots showing the variation of effective Young's moduli with *t* and *r* for the five pentagonal tessellations. Plots b) and c) show extracts of the same data for a specific range of geometries. In the plots b) *t* is varied while *r* is fixed at 3.0 mm and in the plots in c) *r* is varied while *t* is kept constant at 0.3 mm.

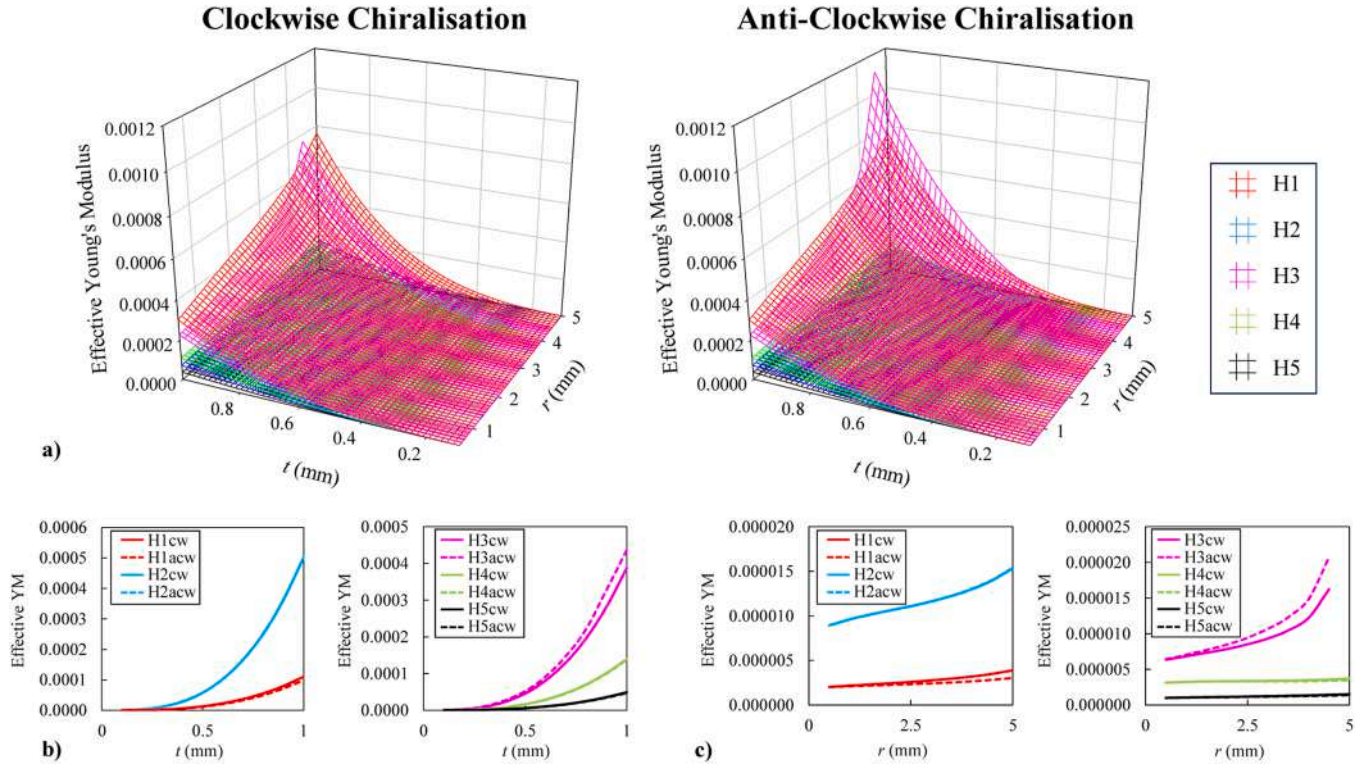


**Fig. 14. a).** Plots showing the variation of effective Young's moduli with *t* and *r* for the five hexagonal tessellations. Plots b) and c) show extracts of the same data for a specific range of geometries. In the plots b) *t* is varied while *r* is fixed at 3.0 mm and in the plots in c) *r* is varied while *t* is kept constant at 0.3 mm.

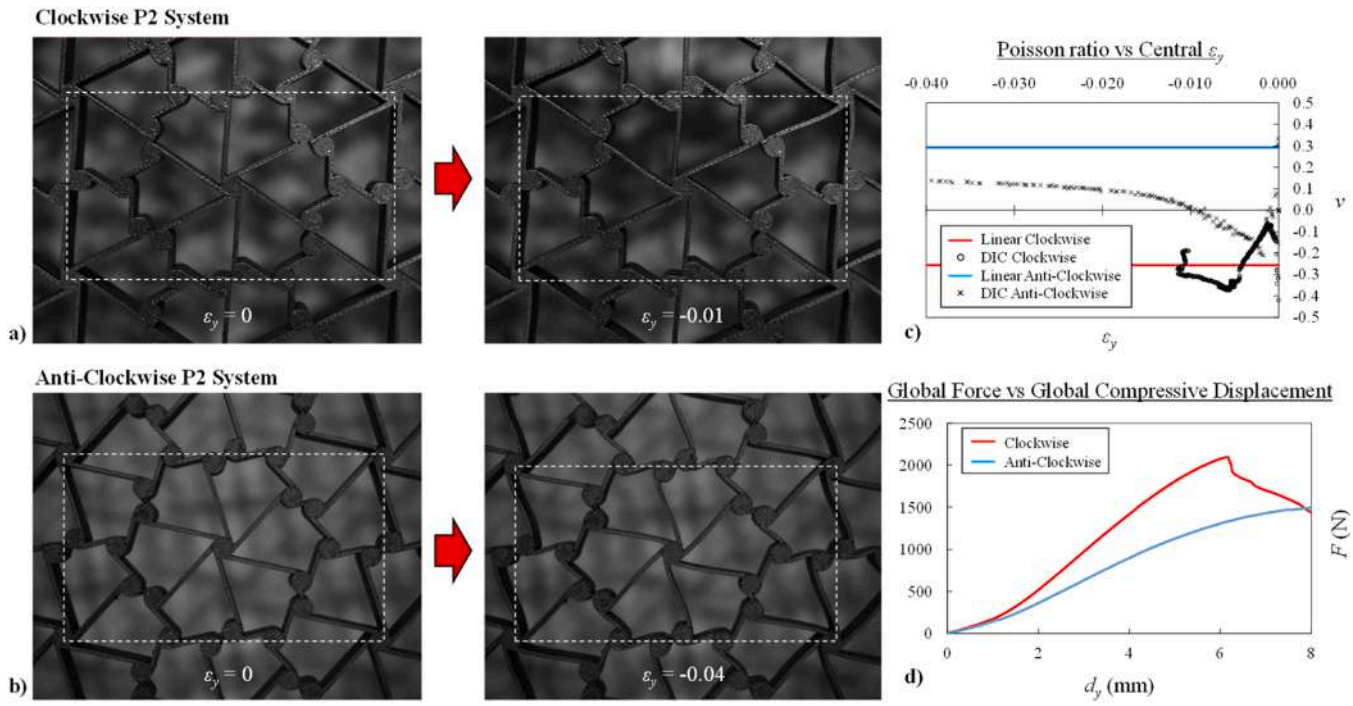


**Fig. 15.** Images showing the undeformed and deformed a) clockwise and b) anti-clockwise chiralised pentagonal tessellations. c) Plot showing the variation of Poisson's ratio over compressive strains for the central RUC obtained through DIC of the experimental prototypes and corresponding linear periodic FE simulations. d) Plots showing the variation in global force with global compressive displacement of the 3D-printed prototypes.

and anti-clockwise chiralised systems were also mirrored in the results obtained from the experimental tests on the 3D-printed prototypes. In the case of the pentagonal tessellation chirals, shown in Fig. 15, it is clearly evident that there are significant differences in the mechanical properties and deformation behaviour of the clockwise and anti-clockwise systems. In the case of the clockwise system (see Fig. 15c), a distinctly negative Poisson's ratio is observed in the range of –0.3, similar to the prediction of the linear FE simulation of the periodic system. On the other hand, the corresponding anti-clockwise, the Poisson's ratio is generally positive over a range of 4 % compressive strain at a value of *ca.* +0.1. This value is slightly lower in magnitude than the predicted value of +0.3 from the linear FE periodic simulation. It is

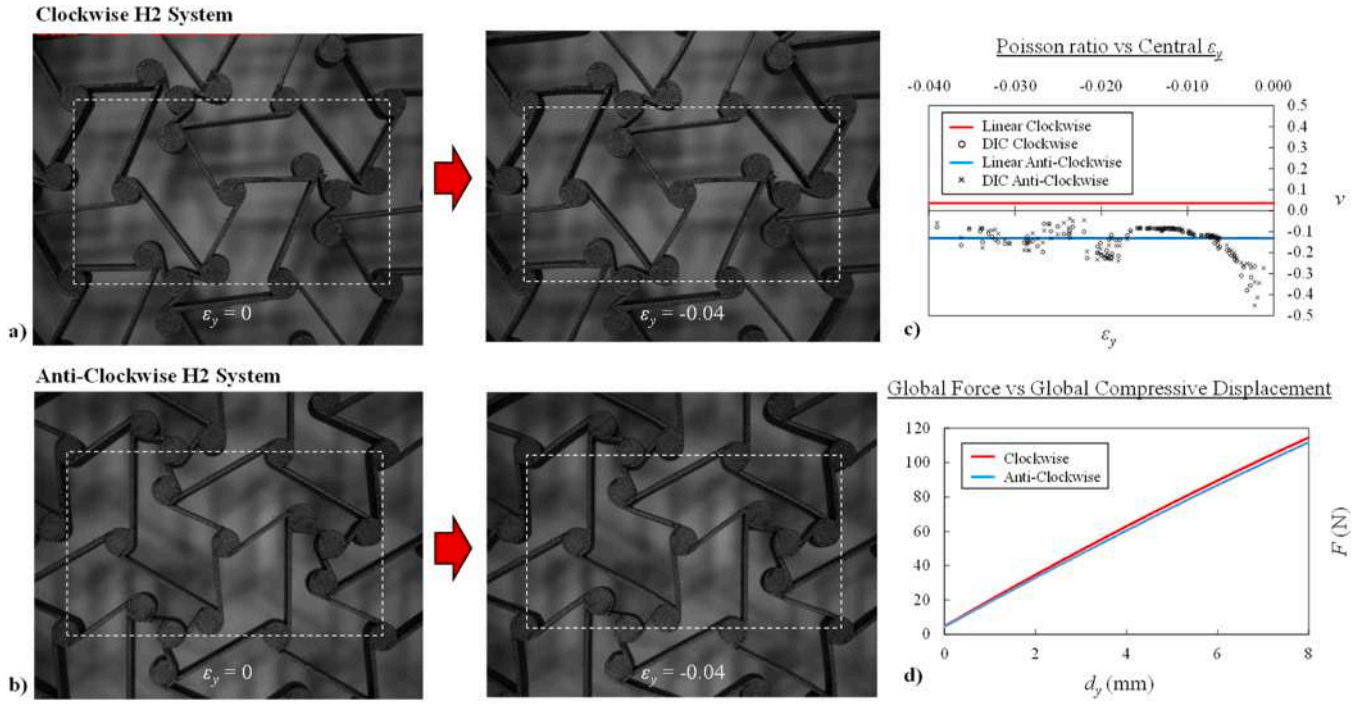


**Fig. 16.** Images showing the undeformed and deformed a) clockwise and b) anti-clockwise chiralised hexagonal tessellations. c) Plot showing the variation of Poisson's ratio over compressive strains for the central RUC obtained through DIC of the experimental prototypes and corresponding linear periodic FE simulations. d) Plots showing the variation in global force with global compressive displacement of the 3D-printed prototypes.

worth noting, that for the clockwise system the deformation of the central RUC was minimal in comparison to the global deformation of the system and, therefore, the Poisson's ratio was measured over a localised strain range of –0.01.

In the case of stiffness, appreciable differences were also observed between the two systems. As shown in Fig. 15d, the clockwise system is significantly stiffer than the anti-clockwise system. This increased stiffness is also accompanied by a decreased strain tolerance, with localised fracture of ligaments at the uppermost region of the prototype being observed at a global displacement of 6 mm (corresponding to a global compressive strain of *ca.* 3 %). On the other hand, the anti-clockwise system exhibits a lower stiffness and did not undergo failure within the applied strain range. These results highlight the difference in mechanical behaviour induced by the direction of chiralisation used to transform these tessellations into chiral metamaterials.

On the other hand, as shown in Fig. 16, the deformation modes and mechanical properties of the hexagonal tessellations are extremely similar. This was to be expected, since as indicated by the parametric

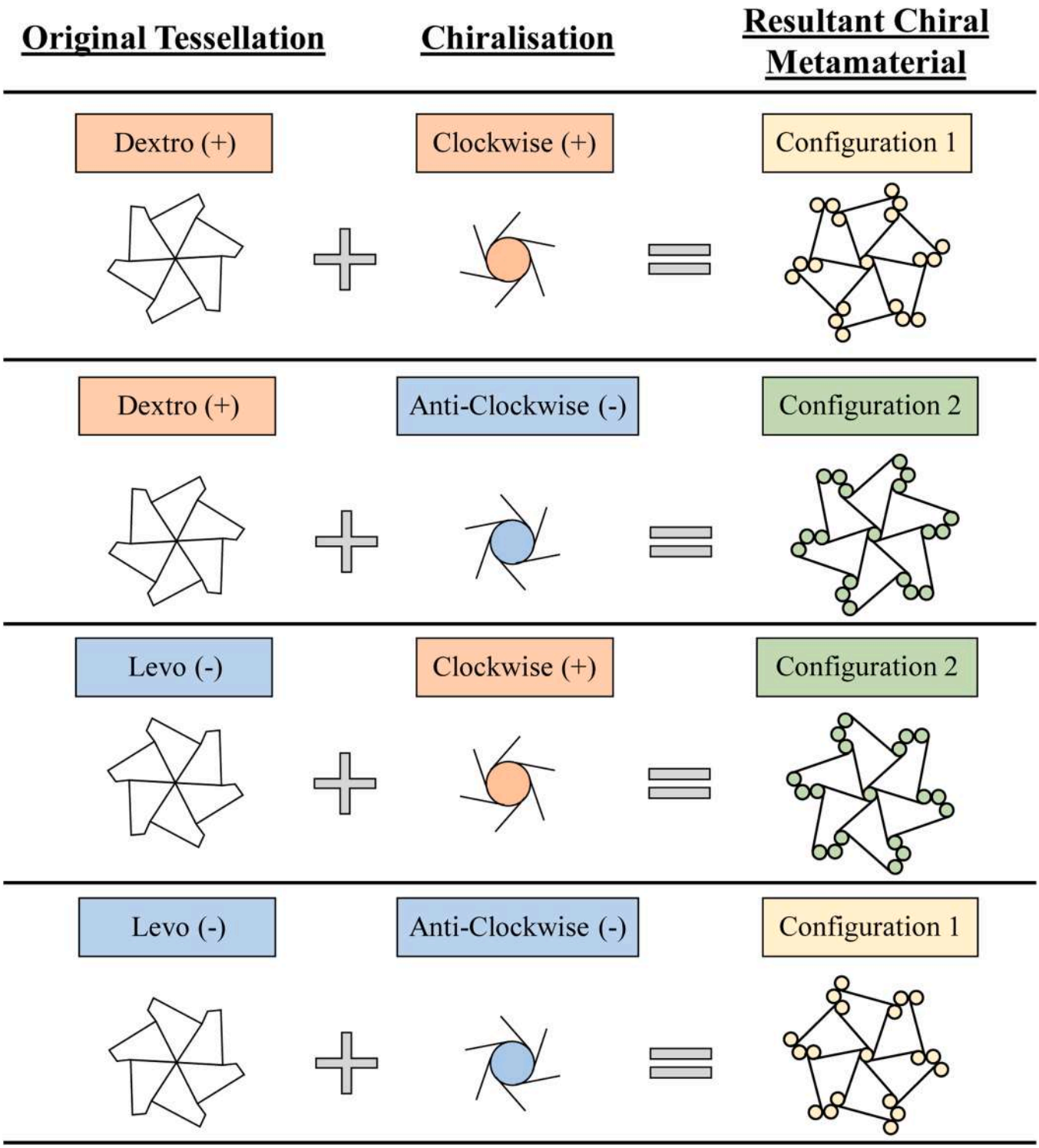


**Fig. 17.** Schematic showing the different combinations of structures which may be obtained by chiralising tessellations which originally possess no axis of symmetry.

simulation run, the influence of chiralisation on the mechanical properties of these systems is minimal and, therefore, the direction of chiralisation is expected have only a minor effect. In fact, both the clockwise and anti-clockwise systems showed similar Poisson's ratios of around –0.1. This is in line with the predictions of the linear periodic FE simulations, which showed a Poisson's ratio of +0.03 for the clockwise chiral system and –0.13 for the anti-clockwise system. This difference is very slight in realistic terms and it can be said that both systems exhibit a *quasi*-zero Poisson's ratio, which is similar to what was observed in the experimental tests. In terms of stiffness, the hexagonal systems also exhibit extremely similar values (see Fig. 16d). It is also worth noting that the global stiffness of both these systems is extremely low in comparison to the pentagonal tessellations despite both systems having the same ligament thickness of 1 mm. This result also corresponds to the observations of the initial parametric simulation run which shows that the pentagonal tessellation chirals are generally stiffer than the corresponding hexagonal tessellation chirals.

The results obtained from both the FE and experimental studies conclusively show that the direction of chiralisation plays a significant role on the deformation modes and mechanical properties of tessellations which do not possess an axis of symmetry. This influence is particularly pronounced in the case of systems in which chiralisation induces a complete change of deformation behaviour such as the Florent pentagonal tessellation studied in this work. In the case of systems which are less affected by chiralisation such as the hexagonal tessellation used in this work, the influence of the direction of chiralisation is less evident, but still noticeable. This observation is congruent with findings from previous studies on chiralised tessellations, where it was observed that tessellations made from higher $n$-sided polygons such as octagons and dodecahedrons are less influenced by chiralisation in comparison to those made from lower $n$-sided polygons such as triangles, quadrilaterals and pentagons [38].

Before concluding, it is important to highlight the fact that the terms clockwise and anti-clockwise used to classify the two directions of chiralisation employed in this work are relative terms which are defined with respect to the original tessellation itself. Since the original tessellation does not possess an axis of symmetry, in geometric terms it can be defined as being already "chiral". If for the sake of convenience, we apply the chemical enantiomeric nomenclature of handedness to the original tessellation and refer to it in terms of levo (-) and dextro (+) chirality, then it is evident that upon chiralisation of these enantiomers in a clockwise and anti-clockwise direction, four resultant metamaterial configurations are possible, of which in reality are two pairs of mirror-images. This point is illustrated in Fig. 17, where it is shown that a dextro-tessellation combined with clockwise chiralisation results in an equivalent metamaterial structure to that of the levo-tessellation combined with anti-clockwise chiralisation. The same applies to a dextro-tessellation combined with an anti-clockwise chiralisation and a levo-tessellation with a clockwise tessellation. In this work, therefore, by keeping the original tessellation fixed at one enantiomeric configuration and varying only the direction of chirality, we have analysed both possible configurations of the resultant chiral metamaterial (1 and 2 in Fig. 17) for each of the tessellations studied.

The work conducted in this study clearly demonstrates the versatility which the chiralisation of Euclidean polygonal tessellation possesses as a method for metamaterial design. Besides allowing for an increased variation of possible mechanical properties, in comparison with traditional chiral metamaterials, courtesy of the high number of geometric design parameters such as tessellation configurations ($i, j, k$), chiral node radius ($r$) and ligament thickness ($t$), a further important design variable has been added in terms of direction of chirality. This new additional design factor, which is applicable only to tessellations which originally do not possess an axis of symmetry, has been shown to have a great influence on the mechanical properties and deformation behaviour of the resultant chiral systems and may potentially be used to obtain combinations of stiffness and Poisson's ratios which may be unattainable from systems which are defined by a single chiralisation direction. It is also worth noting that since this factor applies only to base tessellations which lack an axis of symmetry, traditional well-known chiral honeycombs such as hexachiral, tetrachiral and trichiral honeycombs are not influenced by the direction of chiralisation, hence the reason why this variable has previously not been considered as important in the literature. This means that for a wide range of irregular monohedral and polyhedral tessellations, a wider range of configurations is geometrically available and a systematic analysis of these systems is expected to yield an extremely large spectrum of possible combinations of mechanical properties. Thus, the findings of this work also open up new avenues in the production of chiral auxetic metamaterials since they introduce a new design parameter which was up till now considered irrelevant with respect to its influence on mechanical properties and deformation mode.

## 5. Conclusion

In this work, we analysed the influence of the direction of chiralisation on the mechanical properties and deformation modes of two transversely-isotropic 2D tessellations exhibiting hexagonal and trigonal rotational symmetry. The results obtained indicate that this parameter is an extremely important factor for tessellations which lack an axis of symmetry, meaning that two distinct configurations of chiral metamaterials exhibiting entirely different mechanical properties may be obtained from a single base tessellation depending on the whether clockwise or anti-clockwise chiralisation is applied. It was also shown that the Florent pentagonal tessellation was significantly more affected by this factor in comparison to the trigonal-symmetry hexagonal tessellation. This finding highlights the vast spectrum of geometric versatility provided by the chiralisation of Euclidean tessellations produced from irregular polygons. Despite the strict geometric constraints associated with their intrinsic rotational symmetry, they can be designed from a large variety of geometric parameters which are not available for traditional chiral metamaterials such as hexachiral honeycombs, including the direction of chiralisation.

## CRediT authorship contribution statement

**Luke Mizzi:** Writing – original draft, Software, Methodology, Investigation, Formal analysis, Conceptualization. **Luigi Grasselli:** Writing – review & editing, Validation, Investigation, Conceptualization. **Andrea Spaggiari:** Writing – review & editing, Investigation, Conceptualization.

## Declaration of competing interest

The authors declare that they have no known competing financial interests or personal relationships that could have appeared to influence the work reported in this paper.

## Data availability

Data will be made available on request.

## Appendix 1. – Geometric conditions for the chiralisation of Florent Pentagonal tessellations

As stated previously in Section 2.3, the chiralisation of the Florent Pentagonal tessellations is subject to additional geometric constraints linked to the specific direction of chiralisation. A detailed explanation of these constraints, which were used to obtain the conditions presented in Eq. 9 and 10 of the main manuscript, are provided in this appendix. Both Figures A1 and A2 refer to a generic case of the pentagon illustrated in Fig. 4.

*Clockwise chiralisation*

A generic case of a segment of a clockwise-chiralised tessellation is shown in Fig. A1.

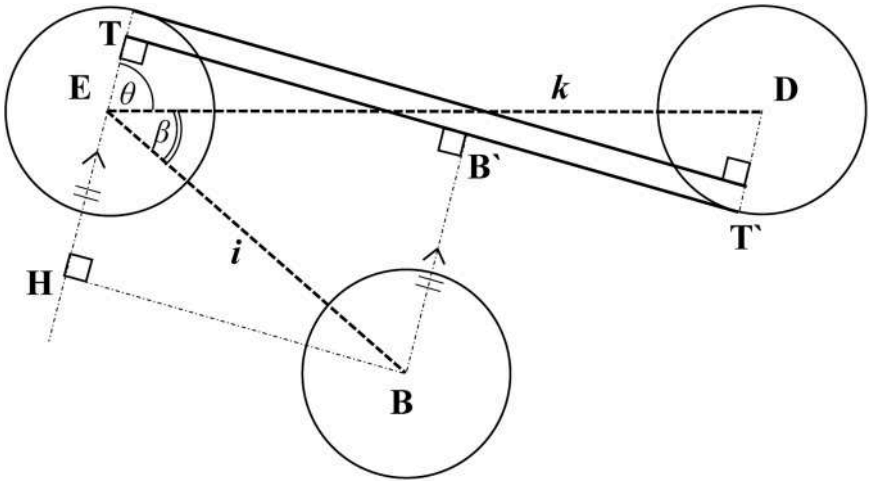


**Fig A1.** Schematic of the clockwise chiralisation of a segment of a generic Florent Pentagonal tessellation including lengths $i$ and $k$.

In order for the chiral metamaterial structure to be realisable, the node with centre point **B** must not intersect with the ligament **TT**′, which in turn means that the side **BB**′ must be greater than the node radius, $r$. This length may be defined as a function of the angles $\theta$ and $\beta$, which are defined as follows:

$$\widehat{TED} = \theta = \arccos\left(\frac{2r - t}{k}\right) \tag{A1}$$

$$\widehat{BED} = \beta = \arccos\left(\frac{i^2 + k^2 - 3j^2}{2ik}\right) \tag{A2}$$

In order for the aforementioned condition to be met, the length **BB**′ can be found as follows:

$$\begin{aligned} BB' &= HT = EH + ET \\ &= i\cos(\pi - (\theta + \beta)) + (r - t) \\ &= -i\cos(\theta + \beta) + r - t \end{aligned} \tag{A3}$$

and hence, since **BB**′ must be greater than $r$, the following condition must be respected:

$$i\cos(\theta + \beta) < -t \tag{A4}$$

*Anti-clockwise chiralisation*

In the case of anti-clockwise chiralisation similar considerations must be followed. As shown in Fig. A2, the situation can still be described by the same parameters as the clockwise case, with the angles $\theta$ and $\beta$ both being defined by the same terms in Eqs. A1 and A2.

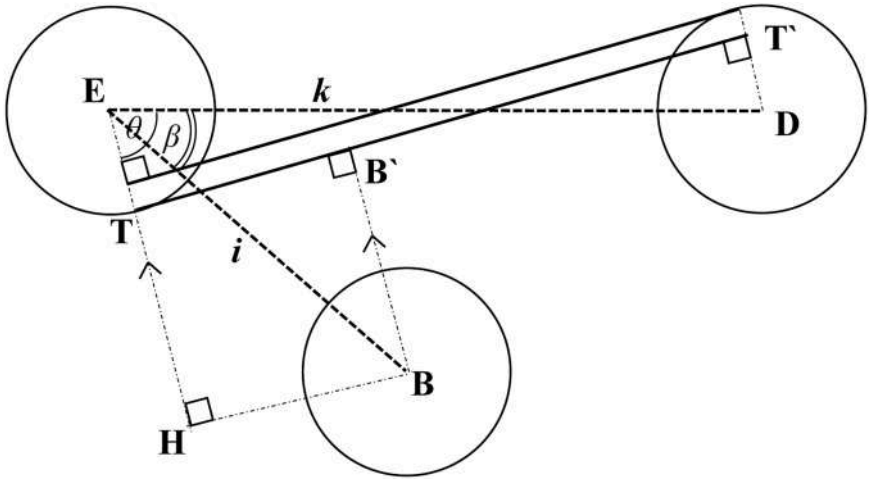


**Fig. A2.** Schematic of the anti-clockwise chiralisation of a segment of a generic Florent Pentagonal tessellation including lengths *i* and *k*.

Even in this case the chiral node with centre B must not intersect with the line **TT′** and, hence, **BB′** must be greater than the node radius, *r*. For anti-clockwise chiralisation, the length **BB′** is defined as follows:

$$\begin{aligned} BB' &= HT = EH - ET \\ &= i\cos(\theta - \beta) - r \end{aligned} \tag{A5}$$

and hence, since **BB′** must be greater than *r*, the final condition is the following:

$$i\cos(\theta - \beta) > 2r \tag{A6}$$

## Appendix 2. – Mesh convergence analysis

In this appendix, the results of mesh convergence studies conducted on representative structures of the Florent pentagonal and trigonal symmetry hexagonal tessellation-based chiral systems are presented (see Fig. A3). The two structures investigated are the following:

P3: $i = j = k = 24$ mm; $t = 0.4$ mm, $r = 3.5$ mm, Clockwise Chiralisation
H1: $i = 24$ mm; $j = 19.2$ mm; $k = 14.4$ mm, $t = 0.4$ mm; $r = 3.5$ mm, Clockwise Chiralisation
Mesh sizes: $t/2$, $t/4$, $t/6$

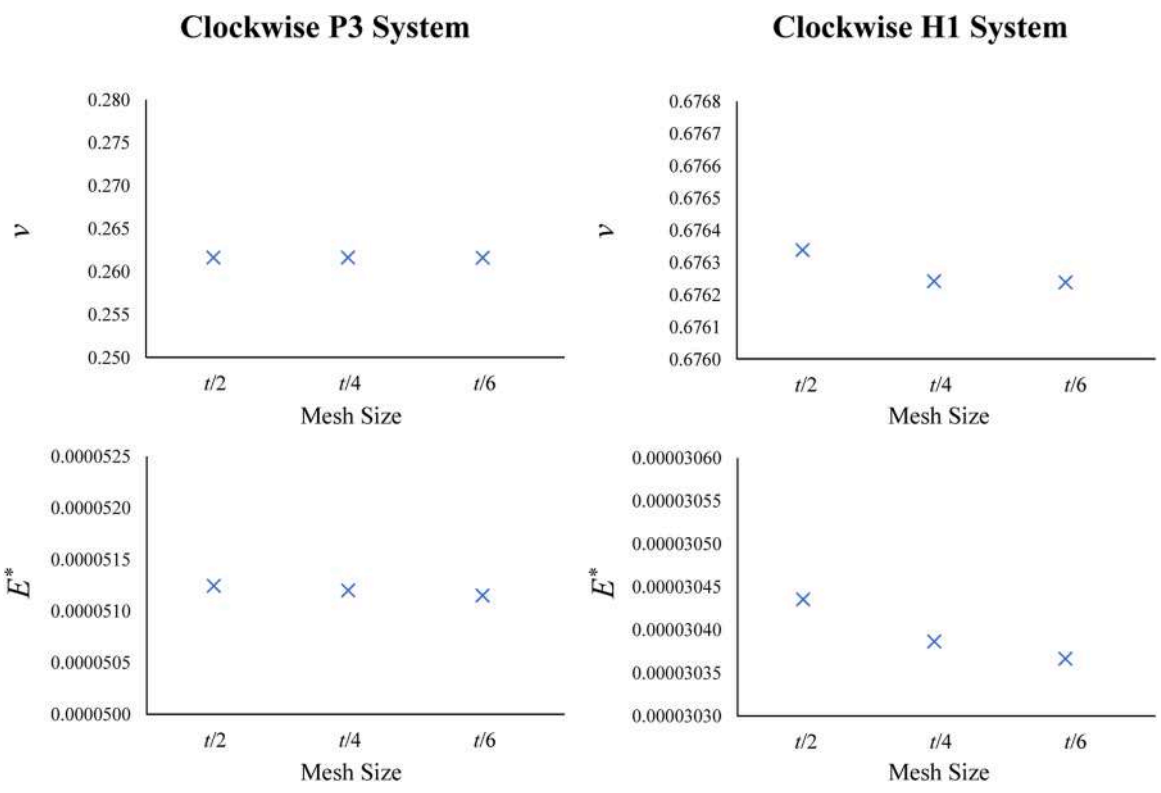


**Fig. A3**Mesh convergence testing plots showing the changes in Poisson's ratios and effective Young's moduli for two structures with different mesh sizes.

It is evident that all mesh sizes utilised exhibit extremely similar results and therefore a mesh size of $t/4$ was chosen in order to achieve optimal accuracy and computational efficiency.

## References


[1] K.E. Evans, M.A. Nkansah, I.J. Hutchinson, S.C. Rogers, Molecular network design, Nature 353 (1991) 124.

[2] T. Li, F. Liu, L. Wang, Enhancing indentation and impact resistance in auxetic composite materials, Compos. B Eng. 198 (2020), https://doi.org/10.1016/j.compositesb.2020.108229.

[3] C. Lira, P. Innocenti, F. Scarpa, Transverse elastic shear of auxetic multi re-entrant honeycombs, Compos. Struct. 90 (2009) 314–322, https://doi.org/10.1016/j.compstruct.2009.03.009.

[4] L. Mizzi, E. Salvati, A. Spaggiari, J.C. Tan, A.M. Korsunsky, Highly stretchable two-dimensional auxetic metamaterial sheets fabricated via direct-laser cutting, Int. J. Mech. Sci. 167 (2020), https://doi.org/10.1016/j.ijmecsci.2019.105242.

[5] S.K. Bhullar, Influence of negative Poisson's ratio on stent applications, Adv. Mater. 2 (2013) 42, https://doi.org/10.11648/j.am.20130203.14.

[6] P. Soman, J.W. Lee, A. Phadke, S. Varghese, S. Chen, Spatial tuning of negative and positive Poisson's ratio in a multi-layer scaffold, Acta Biomater. 8 (2012) 2587–2594, https://doi.org/10.1016/j.actbio.2012.03.035.

[7] L. Mizzi, K.M. Azzopardi, D. Attard, J.N. Grima, R. Gatt, Auxetic metamaterials exhibiting giant negative Poisson's ratios, Phys. Status Solid. - Rap. Res. Lett. 9 (2015) 425–430, https://doi.org/10.1002/pssr.201510178.

[8] S. Huang, Y. Liu, Y. Zhao, Z. Ren, C.F. Guo, Flexible electronics: stretchable electrodes and their future, Adv. Funct. Mater. 29 (2019), https://doi.org/10.1002/adfm.201805924.

[9] Z. Jiao, Z. Hu, Z. Dong, W. Tang, H. Yang, J. Zou, Reprogrammable metamaterial processors for soft machines, Adv. Sci. 11 (2023) 2305501.

[10] K.W. Wojciechowski, Two-dimensional isotropic system with a negative Poisson's ratio, Phys. Lett. a 137 (1989) 60–64.

[11] D. Prall, R.S. Lakes, Properties of a chiral honeycomb with a Poisson's ratio of -1, Int. J. Mech. Sci. 39 (1997) 305–314.

[12] T. Tancogne-Dejean, N. Karathanasopoulos, D. Mohr, Stiffness and strength of hexachiral honeycomb-like metamaterials, J. Appl. Mech., Transact. ASME 86 (2019), https://doi.org/10.1115/1.4044494.

[13] J. Rossiter, K. Takashima, F. Scarpa, P. Walters, T. Mukai, Shape memory polymer hexachiral auxetic structures with tunable stiffness, Smart. Mater. Struct. 23 (2014), https://doi.org/10.1088/0964-1726/23/4/045007.

[14] A. Bacigalupo, M. Lepidi, G. Gnecco, L. Gambarotta, Optimal design of auxetic hexachiral metamaterials with local resonators, Smart. Mater. Struct. 25 (2016) 054009.

[15] K.K. Dudek, New type of rotation of chiral mechanical metamaterials, Smart. Mater. Struct. 29 (2020) 115027.

[16] A. Spadoni, M. Ruzzene, S. Gonella, F. Scarpa, Phononic properties of hexagonal chiral lattices, Wave Motion 46 (2009) 435–450, https://doi.org/10.1016/j.wavemoti.2009.04.002.

[17] F. Scarpa, S. Blain, T. Lew, D. Perrott, M. Ruzzene, J.R. Yates, Elastic buckling of hexagonal chiral cell honeycombs, Compos. Part a Appl. Sci. Manuf. 38 (2007) 280–289, https://doi.org/10.1016/j.compositesa.2006.04.007.

[18] Y.J. Chen, F. Scarpa, Y.J. Liu, J.S. Leng, Elasticity of anti-tetrachiral anisotropic lattices, Int. J. Solid. Struct. 50 (2013) 996–1004, https://doi.org/10.1016/j.ijsolstr.2012.12.004.

[19] K.F. Tee, A. Spadoni, F. Scarpa, M. Ruzzene, Wave propagation in auxetic tetrachiral honeycombs, J. Vib. Acoust. 132 (2010) 0310071–0310078, https://doi.org/10.1115/1.4000785.

[20] X. Lu, V.B.C. Tan, T.E. Tay, Auxeticity of monoclinic tetrachiral honeycombs, Compos. Struct. 241 (2020), https://doi.org/10.1016/j.compstruct.2020.112067.

[21] R. Zhong, M. Fu, Q. Yin, O. Xu, L. Hu, Special characteristics of tetrachiral honeycombs under large deformation, Int. J. Solids. Struct. 169 (2019) 166–176, https://doi.org/10.1016/j.ijsolstr.2019.04.020.

[22] A. Alderson, K.L. Alderson, D. Attard, K.E. Evans, R. Gatt, J.N. Grima, et al., Elastic constants of 3-, 4- and 6-connected chiral and anti-chiral honeycombs subject to uniaxial in-plane loading, Compos. Sci. Technol. 70 (2010) 1042–1048, https://doi.org/10.1016/j.compscitech.2009.07.009.

[23] Y. Pan, X.G. Zhang, D. Han, W. Li, L.F. Xu, Y. Zhang, et al., The out-of-plane compressive behavior of auxetic chiral lattice with circular nodes, Thin-Wall. Struct. 182 (2023) 110152.

[24] A. Alderson, K.L. Alderson, G. Chirima, N. Ravirala, K.M. Zied, The in-plane linear elastic constants and out-of-plane bending of 3-coordinated ligament and cylinder-ligament honeycombs, Compos. Sci. Technol. 70 (2010) 1034–1041.

[25] A. Lorato, P. Innocenti, F. Scarpa, A. Alderson, K.L. Alderson, K.M. Zied, et al., The transverse elastic properties of chiral honeycombs, Compos. Sci. Technol. 70 (2010) 1057–1063, https://doi.org/10.1016/j.compscitech.2009.07.008.

[26] C. Luo, C.Z. Han, X.Y. Zhang, X.G. Zhang, X. Ren, Y.M. Xie, Design, manufacturing and applications of auxetic tubular structures: a review, Thin-Wall. Struct. 163 (2021) 107682.

[27] D. Mousanezhad, B. Haghpanah, R. Ghosh, A.M. Hamouda, H. Nayeb-Hashemi, A. Vaziri, Elastic properties of chiral, anti-chiral, and hierarchical honeycombs: A simple energy-based approach, Theoret. Appl. Mech. Lett. 6 (2016) 81–96, https://doi.org/10.1016/j.taml.2016.02.004.
[28] A.A. Pozniak, K.W. Wojciechowski, Poisson's ratio of rectangular anti-chiral structures with size dispersion of circular nodes, Phys. Status Solid. B Basic Res. 251 (2014) 367–374, https://doi.org/10.1002/pssb.201384256.
[29] R. Gatt, D. Attard, P.S. Farrugia, K.M. Azzopardi, L. Mizzi, J.P. Brincat, et al., A realistic generic model for anti-tetrachiral systems, Phys. Status Solid. B Basic Res. 250 (2013) 2012–2019, https://doi.org/10.1002/pssb.201384246.
[30] W. Wu, X. Song, J. Liang, R. Xia, G. Qian, D. Fang, Mechanical properties of anti-tetrachiral auxetic stents, Compos. Struct. 185 (2018) 381–392, https://doi.org/10.1016/j.compstruct.2017.11.048.
[31] O. Sigmund, S. Torquato, I.A. Aksay, On the design of 1-3 piezo-composites using topology optimisation, J. Mater. Res. 13 (1997) 1038–1048.
[32] Y. Zhu, D. Gao, Y. Shao, H. Chen, C. Yu, Q. Wang, A novel prefabricated auxetic honeycomb meta-structure based on mortise and tenon principle, Compos. Struct. 329 (2024), https://doi.org/10.1016/j.compstruct.2023.117782.
[33] C. Zhang, F. Lu, T. Wei, X. Ling, B. Lin, Y. Zhu, On the collapse stress of tubular enhanced anti-tetra-missing rib structure, Thin-Wall. Struct. 199 (2024), https://doi.org/10.1016/j.tws.2024.111801.
[34] J.N. Grima, R. Gatt, P.S. Farrugia, On the properties of auxetic meta-tetrachiral structures, Phys. Status Solid. B Basic Res. 245 (2008) 511–520, https://doi.org/10.1002/pssb.200777704.
[35] L. Mizzi, A. Spaggiari, Chiralisation of Euclidean polygonal tessellations for the design of new auxetic metamaterials, Mech. Mater. 153 (2021), https://doi.org/10.1016/j.mechmat.2020.103698.
[36] J. Shim, S. Shan, A. Košmrlj, S.H. Kang, E.R. Chen, J.C. Weaver, et al., Harnessing instabilities for design of soft reconfigurable auxetic/chiral materials, Soft. Matter. 9 (2013) 8198–8202, https://doi.org/10.1039/c3sm51148k.
[37] T. Tarnai, P.W. Fowler, S.D. Guest, F. Kovács, Equiauxetic hinged archimedean tilings, Symmet. (Basel) 14 (2022), https://doi.org/10.3390/sym14020232.
[38] L. Mizzi, A. Spaggiari, Novel chiral honeycombs based on octahedral and dodecahedral Euclidean polygonal tessellations, Int. J. Solids. Struct. 238 (2022), https://doi.org/10.1016/j.ijsolstr.2022.111428.
[39] L. Mizzi, A. Simonetti, A. Spaggiari, Mechanical properties and failure modes of additively-manufactured chiral metamaterials based on Euclidean tessellations: an experimental and finite element study, Rapid. Prototyp. J. 30 (2024) 59–71, https://doi.org/10.1108/RPJ-06-2023-0190.
[40] L. Mizzi, L. Grasselli, A. Spaggiari, R. Gatt, P.S. Farrugia, J.N. Grima, Design of isotropic 2D chiral metamaterials based on monohedral pentagonal tessellations, Thin-Wall. Struct. 187 (2023), https://doi.org/10.1016/j.tws.2023.110739.
[41] P.S. Farrugia, R. Gatt, J.N. Grima, A Novel Three-Dimensional Anti-Tetrachiral Honeycomb, Phys. Status Solid. B Basic Res. 256 (2019), https://doi.org/10.1002/pssb.201800473.
[42] K.K. Dudek, A. Drzewinski, M. Kadic, Self-rotating 3D chiral mechanical metamaterials, Proceed. Roy. Soc. 477 (2021).
[43] I. Fernandez-Corbaton, C. Rockstuhl, P. Ziemke, P. Gumbsch, A. Albiez, R. Schwaiger, et al., New twists of 3D chiral metamaterials, Adv. Mater. 31 (2019), https://doi.org/10.1002/adma.201807742.
[44] O. Duncan, M. Chester, W. Wang, A. Alderson, T. Allen, Effect of twist on indentation resistance, Mater. Today Commun. 35 (2023) 105616.
[45] W. Wu, W. Hu, G. Qian, H. Liao, X. Xu, F. Berto, Mechanical design and multifunctional applications of chiral mechanical metamaterials: a review, Mater. Des. 180 (2019) 107950.
[46] T. Frenzel, J. Kopfler, E. Jung, M. Kadic, M. Wegener, Ultrasound experiments on acoustical activity in chiral mechanical metamaterials, Nat. Commun. 10 (2019) 3384.
[47] B. Grünbaum, G.C. Shephard, Tilings by regular polygons, Math. Magaz. 50 (1977) 227–247, https://doi.org/10.1080/0025570x.1977.11976655.
[48] B. Grunbaum, G.C. Shephard, Tilings and Patterns, 2nd Edition, Dover Publishers, New York, 1987.
[49] J.H. Conway, H. Burgiel, C. Goodman-Strauss, The Symmetries of Things, 1st Edition, CRC Press, 2016.
[50] T.C.T. Ting, T. Chen, Poisson's ratio for anisotropic elastic materials can have no bounds, Q. J. Mech. Appl. Math. 58 (2005) 73–82, https://doi.org/10.1093/qjmamj/hbh021.
[51] E. Gao, R. Li, S. Fang, Q. Shao, R.H. Baughman, Bounds on the in-plane Poisson's ratios and the in-plane linear and area compressibilities for sheet crystals, J. Mech. Phys. Solid. 152 (2021), https://doi.org/10.1016/j.jmps.2021.104409.
[52] L. Mizzi, D. Attard, R. Gatt, K.K. Dudek, B. Ellul, J.N. Grima, Implementation of periodic boundary conditions for loading of mechanical metamaterials and other complex geometric microstructures using finite element analysis, Eng. Comput. 37 (2021) 1765–1779, https://doi.org/10.1007/s00366-019-00910-1.